A&A 602, A15 (2017)
DOI: 10.1051/0004-6361/201630113

Astronomy & Astrophysics

The VIMOS Public Extragalactic Redshift Survey (VIPERS)

The decline of cosmic star formation: quenching, mass, and environment connections⋆

O. Cucciati[1,2,⋆⋆], I. Davidzon[3,1], M. Bolzonella[1], B. R. Granett[4,5], G. De Lucia[6], E. Branchini[7,8,9], G. Zamorani[1], A. Iovino[4], B. Garilli[10], L. Guzzo[4,5], M. Scodeggio[10], S. de la Torre[3], U. Abbas[11], C. Adami[3], S. Arnouts[3], D. Bottini[10], A. Cappi[1,12], P. Franzetti[10], A. Fritz[10], J. Krywult[13], V. Le Brun[3], O. Le Fèvre[3], D. Maccagni[10], K. Małek[14], F. Marulli[2,15,1], T. Moutard[16,3], M. Polletta[10,17,18], A. Pollo[14,19], L. A. M. Tasca[3], R. Tojeiro[20], D. Vergani[21], A. Zanichelli[22], J. Bel[23], J. Blaizot[24], J. Coupon[25], A. Hawken[4,5], O. Ilbert[3], L. Moscardini[2,15,1], J. A. Peacock[26], and A. Gargiulo[10]

(Affiliations can be found after the references)

Received 22 November 2016 / Accepted 25 January 2017

ABSTRACT

We use the final data of the VIMOS Public Extragalactic Redshift Survey (VIPERS) to investigate the effect of the environment on the evolution of galaxies between $z = 0.5$ and $z = 0.9$. We characterise local environment in terms of the density contrast smoothed over a cylindrical kernel, the scale of which is defined by the distance to the fifth nearest neighbour. This is performed by using a volume-limited sub-sample of galaxies complete up to $z = 0.9$, but allows us to attach a value of local density to all galaxies in the full VIPERS magnitude-limited sample to $i < 22.5$. We use this information to estimate how the distribution of galaxy stellar masses depends on environment. More massive galaxies tend to reside in higher-density environments over the full redshift range explored. Defining star-forming and passive galaxies through their (NUV$-r$) vs. ($r - K$) colours, we then quantify the fraction of star-forming over passive galaxies, $f_{\rm ap}$, as a function of environment at fixed stellar mass. $f_{\rm ap}$ is higher in low-density regions for galaxies with masses ranging from $\log(\mathcal{M}/\mathcal{M}_\odot) = 10.38$ (the lowest value explored) to at least $\log(\mathcal{M}/\mathcal{M}_\odot) \sim 11.3$, although with decreasing significance going from lower to higher masses. This is the first time that environmental effects on high-mass galaxies are clearly detected at redshifts as high as $z \sim 0.9$. We compared these results to VIPERS-like galaxy mock catalogues based on a widely used galaxy formation model. The model correctly reproduces $f_{\rm ap}$ in low-density environments, but underpredicts it at high densities. The discrepancy is particularly strong for the lowest-mass bins. We find that this discrepancy is driven by an excess of low-mass passive satellite galaxies in the model. In high-density regions, we obtain a better (although not perfect) agreement of the model $f_{\rm ap}$ with observations by studying the accretion history of these model galaxies (that is, the times when they become satellites), by assuming either that a non-negligible fraction of satellites is destroyed, or that their quenching timescale is longer than ∼2 Gyr.

Key words. galaxies: evolution – galaxies: high-redshift – galaxies: statistics – cosmology: observations – large-scale structure of Universe

1. Introduction

Since pioneering work about four decades ago (e.g. Oemler 1974; Davis & Geller 1976; Dressler 1980), environmental studies have increased in importance in the context of galaxy evolution. The first observations found two distinct galaxy populations (red and elliptical vs. blue and spiral) residing in different environments in the local Universe. More recent surveys extended this fundamental result to higher redshifts (e.g. Cucciati et al. 2006; Cooper et al. 2007), and/or replaced the visual or colour classification with estimates of the star formation rate (SFR) or other indicators of the dominant stellar population such as the measurement of the D4000 Å break (see e.g. Balogh et al. 1998; Hashimoto et al. 1998; Gómez et al. 2003; Kauffmann et al. 2004; Grützbauch et al. 2011b).

The environment reconstruction has also been improved over the years. The systematic identification of galaxy clusters and groups allowed the community to perform more detailed analysis of galaxy populations in different environments (see e.g. Cucciati et al. 2010; Iovino et al. 2010; Gerke et al. 2012; Knobel et al. 2013; Kovač et al. 2014; Annunziatella et al. 2014; Haines et al. 2015, and references therein). Furthermore, the development of new methods to compute the local density around galaxies (such as Voronoi tessellation) have enabled both the identification of galaxy clusters and the parameterisation of the density field as a whole to become more reliable (Marinoni et al. 2002; Cooper et al. 2005; Kovač et al. 2010; Lemaux et al. 2016; Fossati et al. 2017). Moreover, the complex topology of the

⋆ Based on observations collected at the European Southern Observatory, Cerro Paranal, Chile, using the Very Large Telescope under programs 182.A-0886 and partly 070.A-9007. Also based on observations obtained with MegaPrime/MegaCam, a joint project of CFHT and CEA/DAPNIA, at the Canada-France-Hawaii Telescope (CFHT), which is operated by the National Research Council (NRC) of Canada, the Institut National des Sciences de l'Univers of the Centre National de la Recherche Scientifique (CNRS) of France, and the University of Hawaii. This work is based in part on data products produced at TERAPIX and the Canadian Astronomy Data Centre as part of the Canada-France-Hawaii Telescope Legacy Survey, a collaborative project of NRC and CNRS. The VIPERS web site is http://www.vipers.inaf.it/

⋆⋆ Corresponding author: O. Cucciati,
e-mail: olga.cucciati@oabo.inaf.it

large-scale structure (LSS) can now be dissected, spanning from the large-scale filamentary cosmic web (e.g. Tempel et al. 2013; Einasto et al. 2014; Alpaslan et al. 2014; Malavasi et al. 2017) to detailed analysis focused on smaller regions (e.g. single clusters or walls, as in Gavazzi et al. 2010; Boselli et al. 2014; Iovino et al. 2016).

In this context, spectroscopic galaxy surveys play a pivotal role in identifying LSS both on small and large scales. Several analyses have used some of the most precise photometric redshifts available to date (Scoville et al. 2013; Darvish et al. 2015; Malavasi et al. 2016). Despite this, spectroscopic measurements of galaxy redshifts ($z_{\rm spec}$) are generally required in order to minimise the uncertainties in the radial position of galaxies. In some cases, the $z_{\rm spec}$ measurement error is so small that the strongest limitation is due to peculiar velocities (Kaiser 1987). Large and deep spectroscopic surveys comprise the best data-sets to study how environment affects galaxy evolution, thanks to their large volume and the long time-span covered. They are, however, very time consuming to assemble.

At present, only the VIMOS Public Extragalactic Redshift Survey (VIPERS, Guzzo et al. 2014) offers the desired combination of large volume ($5 \times 10^7\,h^{-3}$ Mpc^3) and precise galaxy redshifts at $z > 0.5$. VIPERS was conceived as a high-redshift ($0.5 < z < 1.2$) analogue of large local surveys like 2dFGRS (Colless et al. 2001). With respect to other surveys at intermediate redshifts – for example, zCOSMOS (Lilly et al. 2009), which has the same depth as VIPERS – the larger volume covered by VIPERS significantly reduces the effect of cosmic variance (which has important effects in zCOSMOS: see e.g. de la Torre et al. 2010). This allows us to study rare galaxy populations, such as the most massive galaxies, with more solidity (see Davidzon et al. 2013).

Of course we also need an interpretative architecture in which to frame our observations. Fortunately, today we have sophisticated simulations and theoretical models of galaxy formation and evolution at our disposal that can help us in this task, together with simulations of dark matter (DM) halo merger trees. With respect to the observations, these theoretical tools offer us the advantage to study the relationship between baryonic and dark matter, to link galaxy populations at different redshifts (e.g. the problem of finding the progenitors of a given galaxy population), and study the environmental history of galaxies in detail (e.g. Gabor et al. 2010; De Lucia et al. 2012; Hirschmann et al. 2014).

Much progress has been made with simulations in recent years, with larger simulated boxes (see e.g. the Bolshoi simulation, Klypin et al. 2011; and the MultiDark run, Prada et al. 2012), better spatial resolution (e.g. the Millennium II simulation, Boylan-Kolchin et al. 2009), and the implementation of hydrodynamical codes on cosmological volumes (e.g. the EAGLE simulation, Schaye et al. 2015, and the ILLUSTRIS simulation, Vogelsberger et al. 2014). Much effort has also been made to improve semi-analytical models of galaxy formation and evolution (see e.g. Guo et al. 2011; De Lucia et al. 2014; Henriques et al. 2015; Hirschmann et al. 2016). Although several works have studied the role of the environment in models of galaxy evolution (see e.g. Cen 2011; De Lucia et al. 2012; Hirschmann et al. 2014; Henriques et al. 2016), some limitations still remain, such as the environment definition, which has to be linked to observational quantities in order to make a meaningful comparison between the models and real data (see Muldrew et al. 2012; Haas et al. 2012; Hirschmann et al. 2014; Fossati et al. 2015).

As a final note, we remark that the way in which we ask ourselves the questions to be answered has also evolved in recent years. As an example, the wide-spread scenario of "nature vs. nurture" in galaxy evolution has been questioned, and it might well be an ill-posed problem. In fact, even if we possessed an ideal set of simulations and observations, it would be misleading to analyse them by contrasting environmental effects with the evolution driven by intrinsic galaxy properties (such as the stellar or halo mass). These two aspects are physically connected, and it is impossible to fully separate them (see the discussion in De Lucia et al. 2012).

With this picture in mind, we aim at using VIPERS to shed new light on galaxy evolution and environment. In another paper of this series (Malavasi et al. 2017) we show a reconstruction of the cosmic web, while in this paper we present the density field of the final VIPERS sample. Our goal is to study how environment affects the evolution of the galaxy specific star formation rate (sSFR) and compare it with simulations to obtain new insights into the mechanisms that halt star formation (i.e., "quenching"). The paper is organised as follows. In Sect. 2 we briefly describe the VIPERS sample and the mock galaxy catalogues we use in our analysis. In Sect. 3 we present the VIPERS density field, and we show how environment affects galaxy stellar mass and sSFR in Sect. 4. In Sect. 5 we compare our results to a similar analysis performed in the mock galaxy catalogues. We discuss our findings in Sect. 6 and summarise our work in Sect. 7. In the Appendices we give additional details on the reliability of the density field reconstruction, and we show how the final VIPERS density field compares to that reconstructed from VIPERS first data release.

Except where explicitly stated, we assume a flat ΛCDM cosmology throughout the paper with $\Omega_{\rm m} = 0.30$, $\Omega_\Lambda = 0.70$, $H_0 = 70$ km s^{-1} Mpc^{-1} and $h = H_0/100$. Magnitudes are expressed in the AB system (Oke 1974; Fukugita et al. 1996).

2. Data and mock samples

2.1. Data

VIPERS[1] (Guzzo et al. 2014; Scodeggio et al. 2017) has measured redshifts for $\sim 10^5$ galaxies at redshift $0.5 < z \lesssim 1.2$. The project had two broad scientific goals: i) to reliably measure galaxy clustering and the growth of structure through redshift-space distortions; ii) to study galaxy properties at an epoch when the Universe was about half its current age, over a volume comparable to that of large existing local ($z \sim 0.1$) surveys, like 2dFGRS and SDSS.

The VIPERS global footprint covers a total of 23.5 deg^2, split over the W1 and W4 fields of the Canada-France-Hawaii Telescope Legacy Survey (CFHTLS) Wide. Targets were selected to $i_{\rm AB} < 22.5$ from the fifth data release (T0005, Mellier et al. 2008). A colour pre-selection in $(r - i)$ vs. $(u - g)$ was also applied to remove galaxies at $z < 0.5$. Together with an optimised slit configuration (Scodeggio et al. 2009a), this allowed us to obtain a target sampling rate of ∼47% over the redshift range of interest, about doubling what we would have achieved by selecting a purely magnitude-limited sample to the same surface density.

The VIPERS spectroscopic observations were carried out using the VIsible Multi-Object Spectrograph (VIMOS, Le Fèvre et al. 2002, 2003), using the low-resolution Red grism ($R \simeq 220$ over the wavelength range 5500–9500 Å). The number of slits in each VIMOS pointing was maximised using the SSPOC algorithm (Bottini et al. 2005). The typical radial velocity error on the spectroscopic redshift ($z_{\rm s}$) measurement of

[1] http://vipers.inaf.it

a galaxy is $\sigma_z = 0.00054(1+z)$ (see Scodeggio et al. 2017, for more details). A discussion of the survey data reduction and database system is presented in Garilli et al. (2012).

The data used here correspond to the publicly released PDR-2 catalogue (Scodeggio et al. 2017), with the exception of a small sub-set of redshifts (340 galaxies missing in the range $0.6 < z < 1.1$), for which the redshift and quality flags were revised closer to the release date. Concerning the analysis presented here, this has no effect. We retain only galaxies with reliable redshift measurements, defined as having quality flag equal to 2, 3, 4, and 9. The quality flag is assigned to each targeted object during the process of validating redshift measurements, according to a scheme that has been adopted by previous VIMOS surveys (VVDS, Le Fèvre et al. 2005; and zCOSMOS, Lilly et al. 2009). The average confidence level of single redshift measurements for the sample of reliable redshifts is estimated to be 96.1% (Scodeggio et al. 2017). In our case, this selection produces a sample of 74 835 galaxies.

We computed the survey selection function and assigned a set of three weights to each galaxy with a reliable redshift: the colour sampling rate (CSR), the target sampling rate (TSR), and the spectroscopic success rate (SSR). The CSR takes into account the modification of the redshift distribution, $n(z)$, of a purely flux limited catalogue ($i_{AB} < 22.5$) by the colour pre-selection applied to remove galaxies at $z < 0.5$ from the sample. As a consequence, the CSR depends on redshift, and so it smoothly varies from 0 to 1 from $z \sim 0.4$ to $z \sim 0.6$, and it remains equal to 1 for $z \geq 0.6$. The TSR is the fraction of galaxies in the parent photometric catalogue ($i_{AB} < 22.5$ and colour cut) that have a slit placed over them. Finally, the SSR is the fraction of targeted galaxies for which a reliable redshift has been measured. Considering the TSR and SSR together, VIPERS has an average effective sampling rate of ~40%. In our computation, the TSR depends on the local projected density around each target, while the SSR depends on i-band magnitude, redshift, rest-frame colour, B-band luminosity, and the quality of the VIMOS quadrants.

Unless otherwise specified, we use the W1 and W4 samples together as the "VIPERS sample" throughout this paper. We refer to the sample of galaxies with a reliable spectroscopic redshift as defined above as "spectroscopic galaxies", and to all the other galaxies with only a photometric redshift and with $i < 22.5$ as "photometric galaxies". We refer to the entire flux limited catalogue limited at $i_{AB} < 22.5$, before the colour pre-selection, as the "parent photometric catalogue".

2.2. Photometric redshifts, luminosities, and stellar masses

As part of the VIPERS Multi-Lambda Survey (VIPERS-MLS[2], see Moutard et al. 2016a, for further details), photometry from the final CFHTLS[3] release (T0007[4]) in the *ugriz* filters was optimised to provide both accurate colours and reliable pseudo-total magnitudes. From this photometry, photometric redshifts (z_p) were computed for all galaxies in the VIPERS photometric catalogue. Far-UV (FUV) and near-UV (NUV) from GALEX (Martin & GALEX Team 2005), *ZYJHK* filters from VISTA (Emerson et al. 2004), and K_s from WIRCam (Puget et al. 2004) were also used, when available. *ZYJHK* observations are part of VIDEO (Jarvis et al. 2013). Down to $i_{AB} < 22.5$, the photometric redshift error is $\sigma_{z_p} = 0.035(1+z)$, with a <2% of outliers rate (see Fig. 12 in Moutard et al. 2016a).

Absolute magnitudes, stellar masses, and SFR were obtained through a spectral energy distribution (SED) fitting technique, using the code *Le Phare*[5] as in Moutard et al. (2016b, M16b from now on). The SED fitting used all the photometric bands described above.

We used the stellar population synthesis models of Bruzual & Charlot (2003), with two metallicities ($Z = 0.008$ and $Z = 0.02$) and exponentially declining star formation histories, defined by $SFR \propto e^{-t/\tau}$, with SFR being the instantaneous star formation rate and nine different values for τ, ranging between 0.1 Gyr and 30 Gyr as in Ilbert et al. (2013). We adopted three extinction laws (Prevot et al. 1984; Calzetti et al. 2000; and an intermediate-extinction curve as in Arnouts et al. 2013). We imposed a maximum dust reddening of $E(B-V) \leq 0.5$ for all galaxies and a low extinction for low-SFR galaxies ($E(B-V) \leq 0.15$ if age/$\tau > 4$). We took into account the emission-line contribution as described in Ilbert et al. (2009). To compute the absolute magnitudes, we minimised their dependency on the template library by using the observed magnitude in the band closest to the redshifted absolute magnitude filter, unless the closest apparent magnitude had an error >0.3 mag. We refer to Appendix A.1 of Ilbert et al. (2005) for more details. The SFR assigned to each galaxy is the instantaneous SFR (see above) of the best-fit template at the redshift of the galaxy, and it is not constrained by any prior. From the stellar mass $\mathcal{M}$ and the SFR we also derived the specific SFR (sSFR), defined as $sSFR = SFR/\mathcal{M}$. We computed absolute magnitudes and stellar masses with the same method for both the spectroscopic and photometric galaxies, using their z_s and z_p, respectively.

2.3. Mock samples

We make use of mock galaxy catalogues to test the reliability of the density field reconstruction, and to investigate the physical processes taking place in different environments by comparing how environment affects galaxy evolution in the model and in the data.

Our mock galaxy catalogues were obtained by embedding the semi-analytical model (SAM) of galaxy evolution described in De Lucia & Blaizot (2007) within DM halo merging trees extracted from the Millennium Simulation (Springel et al. 2005). The mass of the DM particles is $8.6 \times 10^8\ h^{-1}\ M_\odot$. The DM run adopted a ΛCDM cosmology with $\Omega_m = 0.25$, $\Omega_b = 0.045$, $h = 0.73$, $\Omega_\Lambda = 0.75$, $n = 1$, and $\sigma_8 = 0.9$. These SAM mock catalogues contain, among other galaxy properties, the right ascension, declination, redshift (including peculiar velocity), i-band observed magnitude, B-band absolute magnitude, galaxy stellar mass, and SFR. We remark that this cosmology is outdated, with for instance σ_8 based on the first-year results of the *Wilkinson* Microwave Anisotropy Probe (WMAP1, Spergel et al. 2003) being larger than more recent measurements such as WMAP7 (Komatsu et al. 2011) and WMAP9 (Hinshaw et al. 2013), where they find σ_8 to be of the order of 0.8. Davidzon et al. (2016) showed that the density distribution is slightly different in two simulations based on the cosmologies from WMAP1 and WMAP3, but WMAP3 had a very low σ_8 ($\sigma_8 = 0.7$). Given that σ_8 (and also other cosmological parameters) from WMAP7 and WMAP9 is closer to that of WMAP1, we do not expect a large difference between simulations based on

[2] http://cesam.lam.fr/vipers-mls/
[3] http://www.cfht.hawaii.edu/Science/CFHTLS/
[4] http://terapix.iap.fr/cplt/T0007/doc/T0007-doc.html
[5] http://www.cfht.hawaii.edu/~arnouts/LEPHARE/lephare.html

WMAP1 or WMAP7 and WMAP9, as also shown in Guo et al. (2013).

We used 50 pseudo-independent light cones, each covering an area corresponding to the VIPERS W4 field, from which we built mock galaxy catalogues, as follows.

- First, from each light cone we extracted a purely flux-limited catalogue with the same magnitude cut as VIPERS ($i \leq 22.5$). We refer to these catalogues as "reference mock catalogues" (RMOCKS from now on). In the RMOCKS we retained the apparent redshift (cosmological redshift plus peculiar velocity) without adding any redshift measurement error. The density contrast computed with these catalogues (δ^R) is the standard on which we assess how well we can measure δ in a VIPERS-like survey.
- Second, from each RMOCK we built two catalogues: a VIPERS-like photometric catalogue, and a VIPERS-like spectroscopic catalogue. The photometric catalogue was obtained by mimicking the VIPERS photometric redshift measurement error by adding a random value extracted from a Gaussian distribution with $\sigma_{zp} = 0.035(1 + z)$ to the apparent redshift of the RMOCK. The spectroscopic catalogue was obtained from the RMOCK first by modelling the $n(z)$ at $z < 0.6$ to mimic the VIPERS CSR, then by applying the same slit-positioning software (SSPOC, see Bottini et al. 2005) as was used to select VIPERS targets. In this way, we were able to obtain the same VIMOS footprint as in VIPERS (see Fig. A.1) and a TSR that varied between quadrants as in VIPERS. We did not model the SSR in the mock catalogue because it depends on a large variety of factors, such as redshift and magnitude. Nevertheless, to account for its net effect of reducing the final number of measured spectroscopic redshifts, we randomly removed some of the galaxies left after applying SSPOC, in order to reach the same average SSR as the VIPERS data. Finally, we mimicked the VIPERS spectroscopic redshift error by adding a random value extracted from a Gaussian distribution with $\sigma_z = 0.00054(1 + z)$ to the apparent redshift. We refer to these photometric and spectroscopic mock catalogues as "VIPERS-like mocks" (VMOCKS from now on).

3. VIPERS density field

We parameterised the local environment around each galaxy using the density contrast δ, which is defined as

$$\delta(\boldsymbol{r}) \equiv \frac{\rho(\boldsymbol{r}) - \langle\rho(\boldsymbol{r}(z))\rangle}{\langle\rho(\boldsymbol{r}(z))\rangle}, \quad (1)$$

where $\rho(\boldsymbol{r})$ is the local density at the comoving position $\boldsymbol{r}$ of each galaxy and $\langle\rho(\boldsymbol{r}(z))\rangle$ is the mean density at that redshift. We estimate $\rho(\boldsymbol{r})$ using counts-in-cells, as follows:

$$\rho(\boldsymbol{r}) = \sum_i \frac{F(\boldsymbol{r}, R)}{\phi_i\,(m, z, \mathrm{RA}, \mathrm{Dec}...)}. \quad (2)$$

In Eq. (2) the sum runs over all the galaxies of the sample used to trace the density field. We call these galaxies "tracers". $F(\boldsymbol{r}, R)$ is the smoothing filter (with scale R) over which the density is computed, and ϕ is the selection function of the sample. We always work in redshift space. In this work we use the fractional density perturbation δ, but we often refer to it simply as "density" for the sake of simplicity.

The computation of ρ depends on a variety of options regarding the filter shape, the sample of galaxies to be used as tracers, how to take into account the spectroscopic sampling rate, etc. These choices are normally the result of a compromise between the characteristics of the survey and the scientific goal. We refer to Kovač et al. (2010), for example, for an extensive discussion of these alternatives. See Appendix A for a detailed discussion of our specific calculation for VIPERS and of the tests we have made to quantify the reliability of our calculation.

We use the density field computed with cylindrical top-hat filters with a half-length of $1000\,\mathrm{km\,s^{-1}}$ and radius corresponding to the distance to the fifth nearest neighbour ("n.n." from now on), using a volume-limited sample of tracers with a luminosity cut given by $M_B \leq -20.4 - z$. This luminosity limit makes the tracer sample complete up to $z = 0.9$, and (more importantly) this selection empirically yields a comoving number density that does not evolve, so that the meaning of our densities is not affected by discreteness effects that change with redshift. Cylinders are centred around all of the galaxies in our sample. With this cylindrical filter, both $\rho(\boldsymbol{r})$ and $\langle\rho(\boldsymbol{r}(z))\rangle$ have the dimensions of surface densities in redshift slices of $\pm 1000\,\mathrm{km\,s^{-1}}$ centred on the redshift of the galaxy around which we compute $\rho(\boldsymbol{r})$.

Figure 1 shows a 2D view of the VIPERS density field (in RA and redshift) computed using the cylindrical counts-in-cells method. Although we apply boundary corrections to the density field computation (see Appendix A), in the present work we only use galaxies for which at least 60% of the cylinder is within the survey footprint (gaps and boundaries) presented in Fig. A.1.

With cylindrical filters we can mitigate the peculiar velocities of galaxies in high-density regions (for example, non-linear redshift space distortions in galaxy clusters), and by using a volume-limited sample we measure the environment with the same tracer population at all explored redshifts. Finally, we chose cylinders with an adaptive radius to reach the smallest possible scales at least in high-density regions, because it is expected that the physical processes affecting galaxy evolution mainly occur on relatively small-scale overdensities.

We measured the projected distance to the fifth n.n. ($D_{\mathrm{p},5}$), which we used to compute the density field. For our volume-limited tracers, $D_{\mathrm{p},5}$ is roughly constant with redshift. For the volume-limited tracers limited at $M_B \leq -20.4 - z$, we find $D_{\mathrm{p},5} \sim 5.5,\ 3.5,\ 3.2,\ 2.0\,h^{-1}$ Mpc for $1 + \delta = 0.50,\ 1.74,\ 2.10$, and 5.30, respectively. These density values correspond to the following key values: $1 + \delta = 0.50$ and 2.10 are the median values for galaxies in voids and for all VIPERS galaxies (see Fig. 2), while $1 + \delta = 1.74$ and 5.30 are the thresholds used here to define low-density and high-density environments (see Sect. 4).

We verified that, as expected, $D_{\mathrm{p},5}$ increases for brighter tracers, at fixed δ. This is our primary motivation for restricting our analysis to redshifts below $z = 0.9$ instead of extending it out to $z = 1$ using even brighter tracers at the price of computing the density field on much larger scales. We also verified that although VIPERS and zCOSMOS have the same flux limit, in VIPERS the distance to the fifth n.n. is larger than in zCOSMOS because of its lower sampling rate and larger photometric redshift error.

As a sanity check, we verified the typical local density as measured for galaxies in groups and in voids. Groups are identified in the flux-limited sample using a Voronoi-Delaunay-based algorithm as described in Iovino et al. (in prep.). Here we distinguish between groups with fewer than or at least six members. Galaxies in voids are identified as galaxies located in the central region of spherical voids with radius $\gtrsim 10.2\,h^{-1}$ Mpc and whose distance from the closest galaxy is $\gtrsim 9.8\,h^{-1}$ Mpc. The void-finding algorithm is the same as presented in Micheletti et al. (2014), but applied to the final

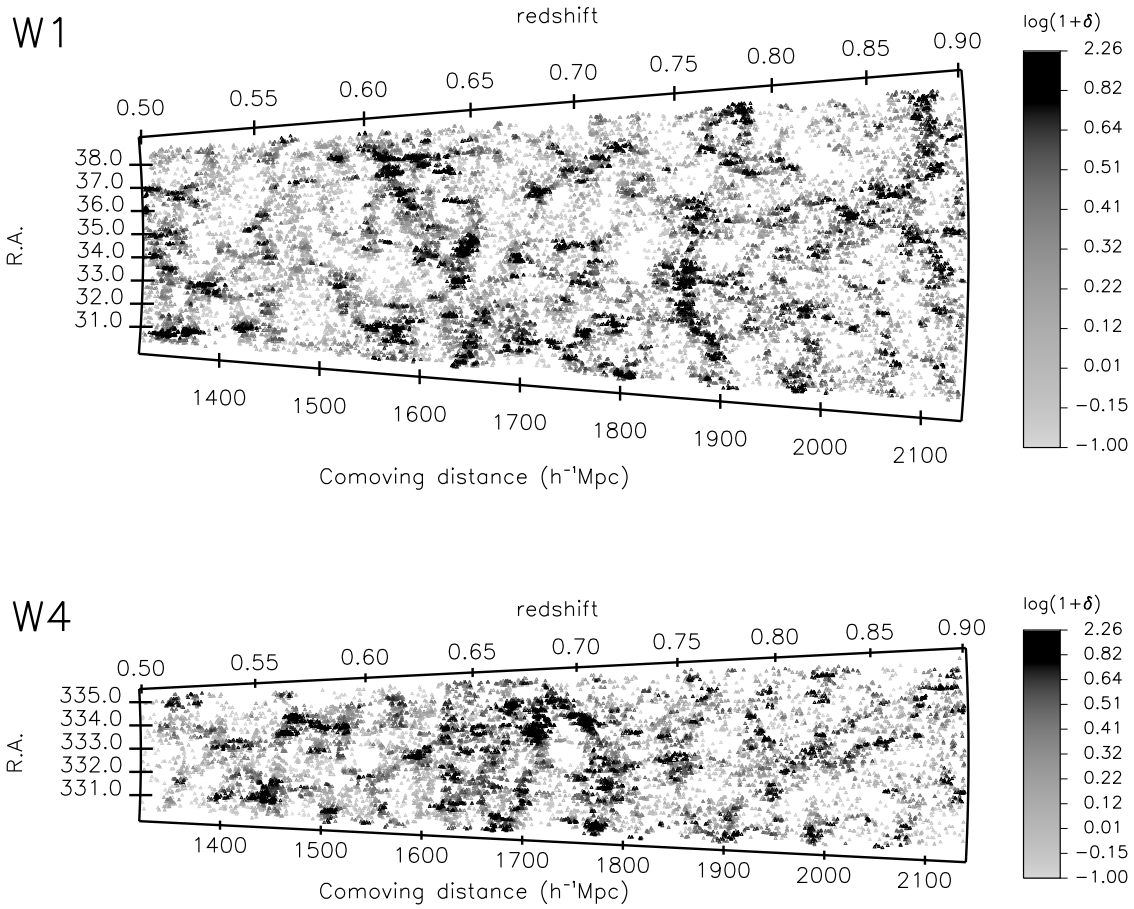

Fig. 1. RA $-z$ distribution of secure-redshift galaxies in W1 (*top*) and W4 (*below*), in comoving coordinates. For the sake of clarity, only the central degree in Dec is plotted. The colour used for each galaxy refers to the value of the local density computed around the galaxy (from light grey for the lowest density to black for the highest density, as in the colour bar). The density is computed in cylindrical filters with radius corresponding to the fifth n.n., using the volume-limited sample of tracers that is complete up to $z = 0.9$.

VIPERS sample. We also refer to Hawken et al. (2017) for a study of voids in VIPERS.

The density distributions for all VIPERS galaxies and for galaxies in groups and voids are shown in Fig. 2 for three redshift bins. At all redshifts, the high-density tail is mostly populated by galaxies in groups, and the richest groups tend to reside in the highest densities (90% of the richest groups members fall in the tail of the ∼40% highest densities). In contrast, as expected, galaxies in voids are most often found in the lowest densities, with 90% of void galaxies residing in the ∼15% of the lowest densities. This better agreement with void galaxies than with group galaxies is expected. In fact, $D_{\rm p,5}$ in low densities is comparable with the typical dimension of voids, while in the highest densities it is still too large to be comparable with the small dimensions of galaxy groups and clusters (see above).

In Fig. 2 we also observe that there is no significant evolution of the density distribution. Kovač et al. (2010) showed that in the zCOSMOS bright sample there is also only a mild evolution of the density distribution, and it is mostly seen moving to $z < 0.4$.

4. Dependence of stellar mass and sSFR on the local density

We wish to study whether and how the stellar mass and SFR depend on environment, and whether any dependence evolves with redshift in the range probed by VIPERS. In particular, we focus on (a proxy of) the sSFR.

We consider the three redshift bins $0.51 < z \leq 0.65$, $0.65 < z \leq 0.8$, and $0.8 < z \leq 0.9$, which were chosen because their median redshifts are nearly equally spaced in time (with time steps of 0.6–0.7 Gyr). In each of these bins, we consider the VIPERS sample to be complete in stellar mass above a given mass limit $\mathcal{M}_{\rm lim}$, namely the mass limit for passive galaxies as defined in Pozzetti et al. (2010). This limit corresponds to $\log(\mathcal{M}_{\rm lim}/\mathcal{M}_\odot) = 10.38$, 10.66, and 10.89 in the three redshift bins, respectively.

We selected a sub-sample of galaxies with stellar mass above the highest mass limit ($\log(\mathcal{M}_{\rm lim}/\mathcal{M}_\odot) = 10.89$) in the entire redshift range $0.51 \leq z \leq 0.9$. We used the first and fourth quartiles of the density distribution of these galaxies as thresholds to define the low-density ("LD") and high-density ("HD") environments: LD galaxies are defined by $1 + \delta \leq 1.74$, and HD galaxies by $1 + \delta \geq 5.30$. These values are very similar to those used in Davidzon et al. (2016, D16 from now on), where they have been derived from an earlier smaller VIPERS data set (the first VIPERS public release, PDR-1) and with a different SED fitting technique. This confirms the consistency between the density field computed for the PDR-1 and the density field computed for the final VIPERS sample (see Appendix B for a quantitative comparison).

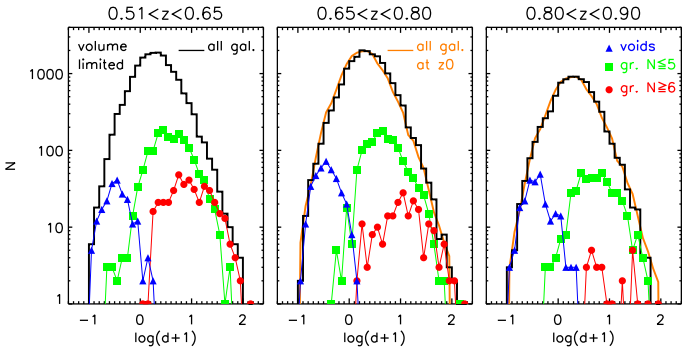

Fig. 2. Density distribution of the VIPERS galaxies in three redshift bins (three columns) for the entire sample (black histogram), for galaxies in voids (blue triangles), in groups with at most five members (green squares), and in groups with at least six members (red circles). See the text for the definition of groups and voids. The density field is computed with cylindrical filters, with a radius given by the fifth n.n. using the volume-limited tracers, which are complete up to $z = 0.9$. To facilitate comparison, in the second and third redshift bins the orange line is the density distribution of the entire sample in the first redshift bin, normalised to the total number of galaxies in each bin.

The average projected distance $D_{p,5}$ to the fifth n.n. for $1+\delta = 1.74$ and $1+\delta = 5.30$ is ∼3.5 and ∼2.0 h^{-1} Mpc, respectively (see Sect. 3).

4.1. Passive and active galaxies

We use the colour-colour diagram (NUV−r) vs. ($r - K$), NUVrK, to define passive and star-forming ("active", from now on) galaxy populations. In this diagram, first described in Arnouts et al. (2013), the (NUV−r) colour is the main tracer of recent star formation (SF); in contrast, the ($r - K$) colour is less sensitive to SF than (NUV−r). ($r - K$) traces the inter-stellar medium absorption, allowing us to separate quiescent and dusty galaxies, which show the same red colours in a classical single-colour distribution (see e.g. Moresco et al. 2013). We consider a galaxy to be passive when

$$\begin{aligned} &(\mathrm{NUV} - r) > 3.73, \quad \text{and} \\ &(\mathrm{NUV} - r) > 1.37 \times (r - K) + 3.18, \quad \text{and} \\ &(r - K) < 1.35. \end{aligned} \tag{3}$$

These boundaries follow the definition provided by D16 (their Eq. (2)), although the values of our thresholds have been slightly modified (by −0.02 and +0.05 mag for the (NUV−r) and ($r - K$) colours, respectively) to take into account small differences in the absolute magnitude estimates[6].

To maximise the difference between the galaxy populations, we decided to exclude the galaxies that have intermediate colours in the NUVrK plane, commonly referred to as "green valley" galaxies, from our analysis. For this reason, our population of active galaxies is not complementary to the passive galaxy population. We set the upper boundary of the active galaxies' locus to be 0.6 mag bluer in NUV − r than the lower boundary of passive galaxies. Our active population is defined as

$$\begin{aligned} &(\mathrm{NUV} - r) < 3.13, \quad \text{or} \\ &(\mathrm{NUV} - r) < 1.37 \times (r - K) + 2.58, \quad \text{or} \\ &(r - K) \geq 1.35. \end{aligned} \tag{4}$$

The condition ($r - K$) > 1.35 (not used in Arnouts et al. 2013) identifies edge-on disc galaxies with a flat attenuation curve. These are the only galaxies that can have such extreme red (r−K) colours (Chevallard et al. 2013; Moutard et al. 2016a). By using this cut in Eqs. (3) and (4), we include these galaxies among the active galaxies. We refer to Fritz et al. (2014) and D16 for a more detailed discussion.

We keep the definitions in Eqs. (3) and (4) constant with redshift. M16b showed that these thresholds depend on redshift, but they can be considered constant in the relatively small redshift range $0.51 < z < 0.9$.

Arnouts et al. (2013) showed that the position of a galaxy in the NUVrK plane correlates with its sSFR. This is also shown in Fig. 2 of D16. We exploit this correlation to facilitate the comparison between our data and the model of galaxy evolution by De Lucia & Blaizot (2007). The light cones we used (see Sect. 2.3) do not have NUV, r, and K absolute magnitudes, but they do have stellar mass and SFR, from which we can compute the sSFR. Practically, we must define some thresholds in sSFR to define the samples of active and passive galaxies in the model. These definitions need to correspond as closely as possible to our classification, which is based on the NUVrK diagram.

It is worthwhile to remark the following. Since the measurement of absolute magnitudes using SED fitting techniques is more accurate than the estimate of the SFR at the level of single galaxies, our primary definition of the active and passive populations is the one based on the NUVrK plane. We also use the definition based on sSFR to facilitate the comparison with the mock catalogues. It is beyond the scope of this paper to investigate the reliability of the SFR derived from the SED fitting in detail (however, see e.g. Conroy et al. 2009).

In Fig. 3 we show the distribution of the sSFR for our sample in the redshift range $0.65 < z < 0.8$ above the mass limit $\log(\mathcal{M}_{\rm lim}/\mathcal{M}_\odot) = 10.66$. About 15–20% of the galaxies in this redshift range and above this mass limit have an sSFR lower than the minimum value in the figure, and therefore their distribution is not plotted for the sake of clarity. For any given value of sSFR, we also show the fraction of passive and active galaxies as defined by Eqs. (3) and (4). The correlation between this definition and the sSFR values is evident. Moreover, we remark that this correlation is not an artefact of the SED fitting procedure: the SFR comes directly from the instantaneous SFR of the best-fit template, while the absolute magnitudes are derived by minimising the template dependence by using the observed magnitude with the closest wavelength (see Sect. 2.2).

Figure 3 shows that the classification of passive and active galaxies based on the NUVrK plane roughly corresponds to $\log(sSFR) < -11.2$ and $\log(sSFR) > -10.8$, respectively. The fractions of active, intermediate, and passive galaxies as a function of the sSFR behave in a similar way in the two other redshift bins considered in this study, therefore we adopt the same sSFR thresholds over the entire redshift range $0.51 < z < 0.9$.

In Fig. 3 we also overplot the sSFR distribution in the Rmocks. The model distribution is different from the data distribution in several aspects. First, the tail of high sSFR is missing in the model. Second, the valley present in the data distribution at $\log(sSFR) \sim -10.8$ appears as a plateau in the model. It also seems to be shifted towards higher values of sSFR. Finally, we

[6] D16 used the code *Hyperz* with a different photometric baseline. Their galaxy templates and the algorithm with which they computed rest-frame magnitudes are also different from M16b.

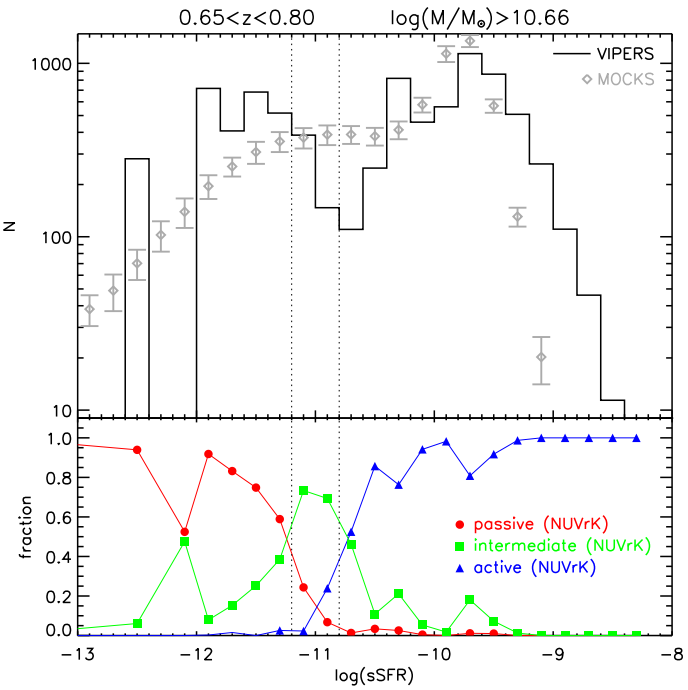

Fig. 3. *Top*: black histogram: distribution of the sSFR ($=SFR/\mathcal{M}$) for the VIPERS galaxies in the redshift range $0.65 < z < 0.8$ and for $\log(\mathcal{M}_{\rm lim}/\mathcal{M}_{\odot}) > 10.66$, which is the completeness mass limit in that redshift range. Diamonds: sSFR distribution in the RMOCKS for galaxies in the same redshift range and above the same mass threshold; the points with the vertical error bars correspond to the average and rms of the 50 mocks catalogues. The sSFR distribution of the RMOCKS is normalised to have the same total number of galaxies as in the VIPERS sSFR distribution. Both the real and simulated distributions have a tail of galaxies with sSFR values below the lowest sSFR limit in this plot, which we do not plot for the sake of clarity. *Bottom*: only for the VIPERS sample (same galaxies as in the top panel), fraction of passive (red circles) and active (blue triangles) galaxies as defined by Eqs. (3) and (4), as a function of their sSFR. We also overplot the fraction of "intermediate" galaxies, i.e. those that do not satisfy the passive or the active definition. The vertical lines at $\log(sSFR) = -11.2$ and $\log(sSFR) = -10.8$ are the thresholds adopted to define passive and active galaxies, respectively, using the sSFR as discussed in Sect. 4.1. These results are very similar in the two other redshift bins (not shown).

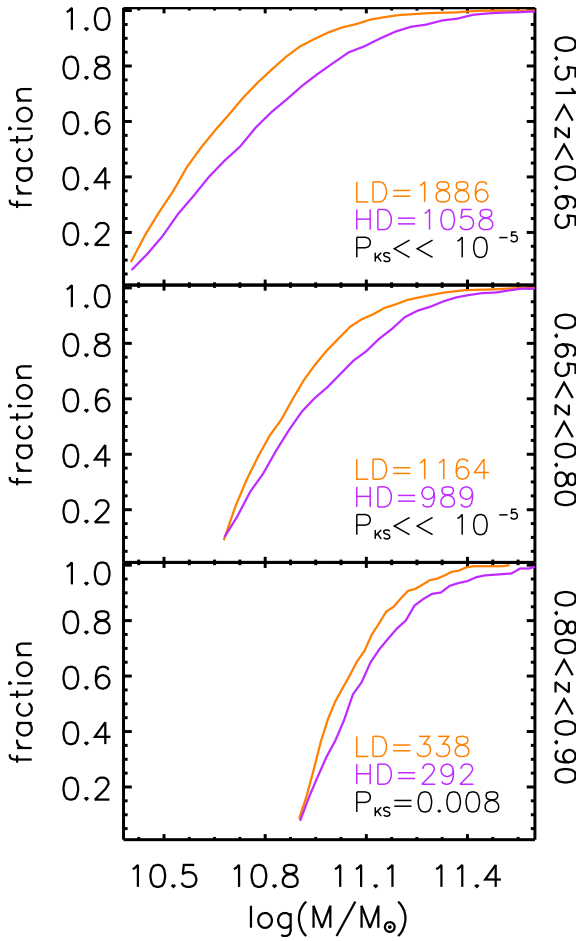

Fig. 4. Stellar mass cumulative distributions in three redshift bins ($0.51 < z \leq 0.65$, $0.65 < z \leq 0.8$, and $0.8 < z \leq 0.9$ *from top to bottom*), for galaxies above the mass limits $\log(\mathcal{M}_{\rm lim}/\mathcal{M}_{\odot}) = 10.38$, 10.66, and 10.89, respectively, in the three redshift bins. Orange lines show the galaxies in LD regions, and violet lines show galaxies in HD regions. The number of galaxies used in each distribution is reported in the corresponding panel. We use all the galaxies above the mass limit, regardless of their NUVrK classification. In each panel we also report the $P_{\rm KS}$ values, i.e. the significance level in a Kolmogorov-Smirnov test for the null hypothesis that the LD and HD distributions are drawn from the same parent distribution.

note that in each redshift bin the tail of the sSFR distribution below the lowest value plotted in the figure comprises about 30% of the model galaxies, but only 15–20% of the VIPERS galaxies. We refer to Appendix C for the analysis of a possible cause of these discrepancies, and to Sect. 5 for the classification of passive and active galaxies in the model.

4.2. Stellar mass segregation in different environments

It is known that galaxy stellar mass correlates with local environment (see e.g. Kauffmann et al. 2004; Scodeggio et al. 2009b). This correlation has been extensively studied in the VIPERS survey in D16 in terms of the galaxy stellar mass function (GSMF) in low- and high-density regions. This dependence can also be qualitatively studied using the cumulative distribution function of the stellar mass. Here we perform such an analysis, primarily as a comparison with other works in the literature that used the same tool. As a second step, we wish to define a set of (narrow) mass bins so that we can study how the environment affects star formation at fixed stellar mass.

Figure 4 shows the cumulative distribution function of galaxy stellar mass in three redshift bins for galaxies above the respective $\mathcal{M}_{\rm lim}$. In each redshift bin, we compare the distributions in the two environments (LD and HD) using a Kolmogorov-Smirnov (KS) test. In all bins we find that the significance level $P_{\rm KS}$ for the null hypothesis, that is, that the two distributions are drawn from the same parent distribution, is of the order of $\ll 10^{-5}$ (with the exception of the highest redshift bin, see below). This excludes the null hypothesis. This is in agreement with the different shapes of the GSMF in LD and HD regions found in D16 (see their Fig. 4).

In more detail, at all explored redshifts the LD distribution rises more rapidly at the lowest masses, while the HD distribution has a more pronounced tail towards the highest stellar masses. This is in agreement with D16, who found that the LD GSMF is steeper at low masses and the high-mass exponential tail of the GSMF is higher in HD regions than in LD regions. Moreover, as in D16, the LD and HD distributions are more similar in the highest redshift bin. We verified that the higher $P_{\rm KS}$ at $z > 0.8$ is partly due to the lower number of galaxies. Reducing

Table 1. Number of active and passive galaxies in each redshift and stellar mass bin for the LD and HD environments.

$\mathcal{M}$ bin [$\log(\mathcal{M}/\mathcal{M}_\odot)$]	Act/pass (LD)	Act/pass (HD)
$0.51 < z < 0.65$		
10.38–10.66	666/243	243/111
10.66–10.89	285/204	137/132
10.89–11.09	102/82	67/96
11.09–11.29	35/41	24/53
11.29–12.00	4/11	7/39
$0.65 < z < 0.80$		
10.66–10.89	365/217	216/199
10.89–11.09	143/149	86/122
11.09–11.29	39/54	51/107
11.29–12.00	4/26	10/48
$0.80 < z < 0.90$		
10.89–11.09	115/73	65/62
11.09–11.29	43/39	28/44
11.29–12.00	11/7	8/20

Notes. Active and passive galaxies are defined according to their position in the NUVrK plane (Eqs. (3) and (4)).

the number of galaxies in the two first redshift bins to make them equal to the third bin increases P_{KS} to a few 10^{-4} at $z < 0.8$. To verify whether the higher P_{KS} at $z > 0.8$ is also due to the smaller mass range explored, we computed P_{KS} at $z < 0.8$ imposing not only the same number of galaxies as at $z > 0.8$, but also the same stellar mass limit $\log(\mathcal{M}_{lim}/\mathcal{M}_\odot) = 10.89$. Reducing the mass range, P_{KS} remains of the order of a few 10^{-4} at $z < 0.8$. This is still lower than P_{KS} at $z > 0.8$. This suggests that the dependence on environment of the high-mass tail of the stellar mass distribution might strengthen with decreasing redshift.

4.3. sSFR as a function of environment

In this section we investigate possible environmental effects on the sSFR (either using the NUVrK definition as a proxy, or the SFR and stellar mass through SED fitting). In particular, we study the ratio of the number of active to passive galaxies, f_{ap}. To separate the role of stellar mass and environment, we need to study how environment affects galaxy evolution at a fixed stellar mass. We did this by dividing our sample into the following narrow mass bins in $\log(\mathcal{M}/\mathcal{M}_\odot)$: 10.38–10.66, 10.66–10.89, 10.89–11.09, 11.09–11.29, and >11.29.

Table 1 shows the number of active and passive galaxies in LD and HD environments in each redshift and mass bin. In the table, active and passive galaxies are defined according to the NUVrK diagram, but the numbers derived using the sSFR definition are very similar.

Below we explain how we built mass-matched samples in the two environments in each mass and redshift bin. This was to further minimise any possible remaining difference in the stellar mass distribution in LD and HD, even in our narrow stellar mass bins.

In each mass and redshift bin, we cut the mass distributions in the two environments so that they have the same minimum and maximum mass value, meaning that they cover exactly the same mass range. Then, in each mass and redshift bin, we (a) take the mass distribution in the environment with the smaller number of galaxies (usually the HD environment) as the reference mass distribution, and (b) we extract 100 samples of galaxies from the mass distribution in the other environment, with the same mass distribution as the reference, allowing repetitions. Each of these 100 samples is constructed to have the same number of galaxies as the reference.

The left panel of Fig. 5 shows f_{ap} as a function of stellar mass in the redshift ranges defined above, separating LD from HD regions. Galaxies are classified as passive and active according to the NUVrK diagram. In each mass bin, we plot f_{ap} obtained by using all the galaxies in the bin (i.e., without applying the mass-matching method). For the environment comprising the highest number of galaxies (LD, with the exception of the highest mass bin) we overplot the average f_{ap} of the 100 mass-matched samples.

When computing f_{ap}, in the original or mass-matched samples, we always weight the galaxies by a factor w that corresponds to the inverse of the total sampling rate, i.e. $w = 1/(\mathrm{CSR} \times \mathrm{TSR} \times SSR)$. However, we verified that our results do not change significantly if we do not use these weights.

We observe the following:

- The median stellar mass values in each mass bin are slightly higher in HD than LD, suggesting that even in the narrow mass bins the mass distribution could be slightly different in the two environments. After the mass-matching, the median stellar mass values approach the median of the opposite environment, as expected. f_{ap} also varies very mildly before and after the mass-matching.
- f_{ap} decreases for higher masses regardless of environment, as expected given the relation between stellar mass and SFR (e.g. Speagle et al. 2014 and Whitaker et al. 2014). The only exception is the highest mass bin at $0.8 < z < 0.9$, where f_{ap} is similar if not higher than in the adjacent mass bin, although uncertainties are large.
- f_{ap} is higher in LD than HD environments, at all masses below $\log(\mathcal{M}/\mathcal{M}_\odot) = 11.29$.
- At fixed stellar mass, f_{ap} slightly decreases with redshift from $z > 0.8$ to $0.65 < z < 0.8$ in both LD and HD, but it ceases to evolve at $z < 0.65$.

These results are in qualitative agreement with those presented in D16, where we separately studied the GSMF as a function of environment for active and passive galaxies. In their Fig. 5, D16 show that the low-mass end is steeper (more negative α) for active galaxies. This corresponds to our f_{ap} increasing for low-mass galaxies. Moreover, at $0.51 < z < 0.65$ the low-mass end of the passive GSMF is much less steep in HD than in LD, which is mirrored by f_{ap} in LD increasing more steeply for lower masses.

On the other hand, we observe that in D16 the ratio of active to passive galaxies should decrease by a factor ~2 from $z \sim 0.85$ to $z \sim 0.55$. Based on the uncertainty on the Schechter parameters of the GSMFs (see their Table 2), this trend is significant to a $\lesssim 2\sigma$ level. We do not observe this redshift evolution in f_{ap}, in agreement with the mild evolution of the passive and active GSMFs in M16b. The main reason why this trend is observed in D16 but not M16b is that they use different SED fitting procedures, which result in different classifications of galaxy type for a fraction of the total sample of galaxies. Although the total GSMFs in the two studies are in excellent agreement with each other, after dividing their sample into active and passive galaxies, M16b found an evolution in number density that is milder than in D16 (see Fig. 14 of M16b and Fig. 3 of D16). As stressed by M16b, we are currently in an era in which large samples decrease random errors, and we can now see the small but dominant systematics produced by different SED fitting estimates. In

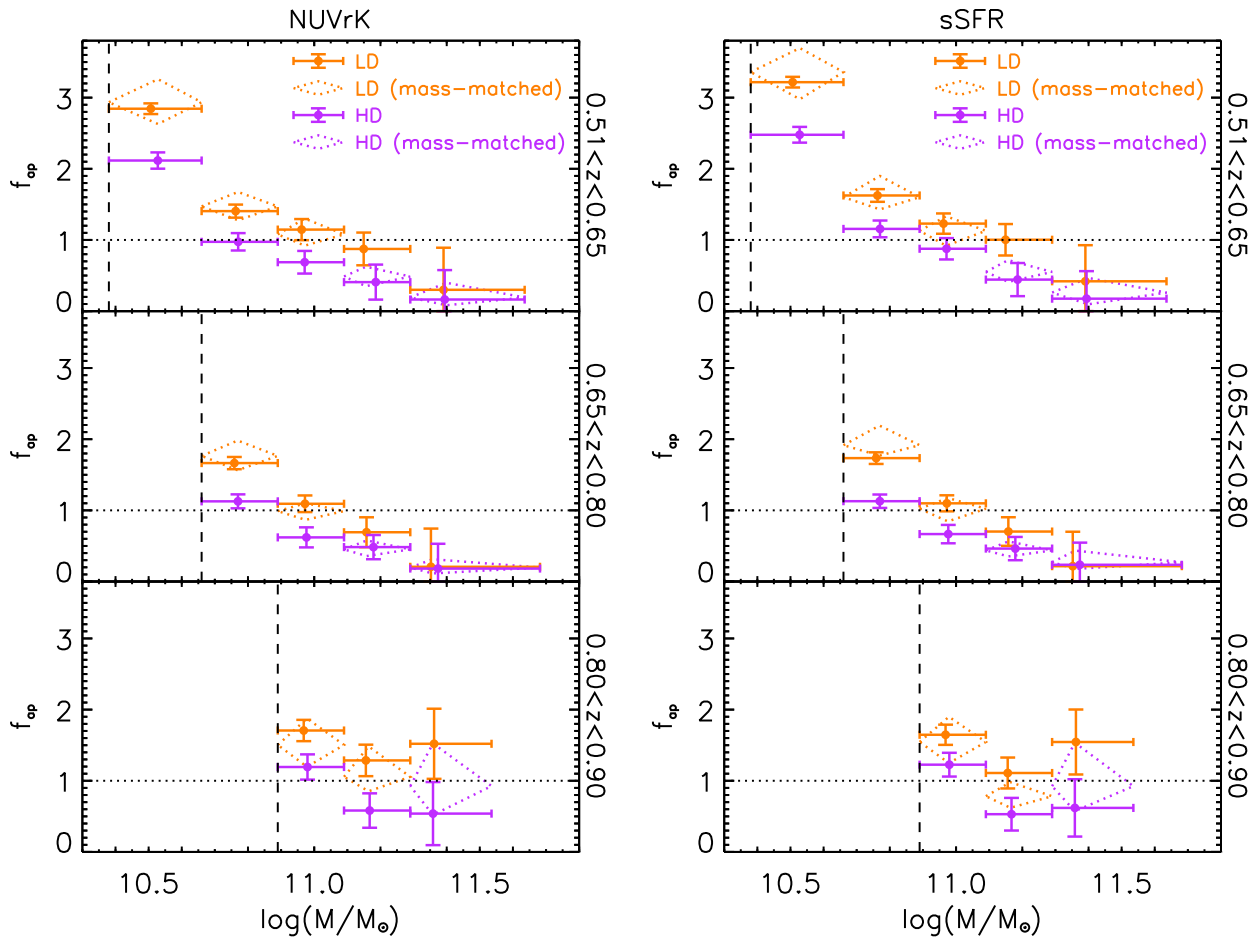

Fig. 5. Ratio of the number of active over passive galaxies ($f_{\rm ap}$) in LD (orange filled circles) and HD (violet filled circles) regions as a function of stellar mass in three different redshift bins. Active and passive galaxies are defined by means of the NUVrK diagram (*left*) or according to their sSFR (*right*). Horizontal error bars indicate the span of the mass bin, and the vertical error bars are derived from the propagation of the Poissonian noise in the counts of active and passive galaxies (if we use the error formula for small samples suggested in Gehrels (1986), the error bars do not change significantly). The x-axis value is the median stellar mass of the sample used to compute $f_{\rm ap}$. Dotted diamonds are for the mass-matched samples in the environment (LD or HD) with more galaxies in each mass and redshift bin. Diamonds are centred on the median $f_{\rm ap}$ value of the 100 mass-matched extractions, and the bottom and top vertices represent the 25% and 75% of the $f_{\rm ap}$ distribution, respectively. The x-axis values is the median of the median stellar mass in each extraction. See text for more details. The vertical dashed line in each redshift bin is the corresponding mass limit $\mathcal{M}_{\rm lim}$. The dotted horizontal line at $f_{\rm ap} = 1$ is for reference.

this case, the differences related to the SED fitting procedure include different CFHTLS photometry (T005 release in D16 and T007 in M16b), more photometric bands used in M16b, and a different SED-fitting code.

Finally, it is worthwhile briefly discussing our findings for the highest stellar mass bin ($\log(\mathcal{M}/\mathcal{M}_\odot) > 11.29$). The number of galaxies at such stellar masses drops steeply, and the error on $f_{\rm ap}$ is very large. For these masses, and at $z < 0.8$, $f_{\rm ap}$ does not appear to depend on environment, but its value is consistent with the general trend of $f_{\rm ap}$ decreasing for higher masses, regardless of environment. At $0.8 < z < 0.9$, in contrast, we do not see a clear dependence of $f_{\rm ap}$ on stellar mass because of the smaller span in stellar mass and the relatively high values of $f_{\rm ap}$ at $\log(\mathcal{M}/\mathcal{M}_\odot) > 11.29$ with respect to the previous mass bins. We defer a more detailed analysis of the properties of very massive galaxies in VIPERS to future work.

As expected by construction, we obtain very similar results (always within 1σ) when we define active and passive galaxies using the NUVrK diagram or the sSFR thresholds, and this is crucial for the comparison with the model.

5. Comparison with the adopted model

We make use of the 50 SAM light cones to study the dependence of $f_{\rm ap}$ on stellar mass, redshift, and environment in the De Lucia & Blaizot (2007) model, and we compare this to real data.

We use the RMOCKS and VMOCKS with two main aims: i) compare $f_{\rm ap}$ in RMOCKS and VMOCKS to verify that the VIPERS selection function does not introduce any spurious signal into our measurement of $f_{\rm ap}$, and ii) compare $f_{\rm ap}$ in the model and in the real data to investigate which physical process(es) could be the cause of the observed environmental trends.

We remark that these mock catalogues cover a smaller volume than the entire VIPERS survey. Each VMOCK has roughly the size of the VIPERS W4 field, which is about one-third of the whole area we probe. For the analysis in this section, we grouped the output (density measurement, sSFR, stellar mass, etc.) of three VMOCKS at a time for a total of 16 larger output catalogues including 48 of the original VMOCKS. This simplifies the comparison with real data because of the similar statistics

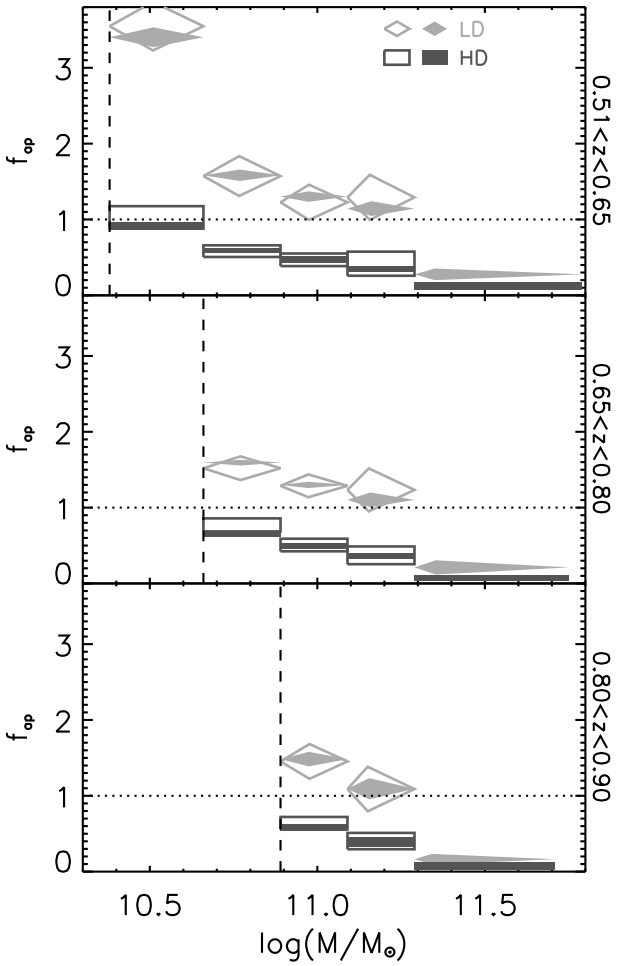

Fig. 6. Ratio of the number of active over passive galaxies (f_{ap}) in LD (light grey) and HD (dark grey) regions in the RMOCKS (filled symbols) and in the VMOCKS (empty symbols) in the same stellar mass bins and redshift ranges as in Fig. 5. In each mass bin, for the environment with fewer galaxies (HD for $\log(\mathcal{M}/\mathcal{M}_\odot) < 11.29$, LD otherwise) we plot f_{ap} as computed directly from the mock catalogues, while for the environment with more galaxies we plot f_{ap} derived from the mass-matched samples. For not mass-matched values, symbols are centred on the y-axis on the mean value of f_{ap} of the 16 mock catalogues, and their height represents the rms around the mean. For mass-matched values, the y-axis position is computed as follows: first we compute the mean f_{ap} of the 100 mass-matched samples in each mock catalogue, then we average the 16 mean values. The height is given by the rms around this mean. For all symbols, the extension on the x-axis indicates the span of the stellar mass bin. For $\log(\mathcal{M}/\mathcal{M}_\odot) > 11.29$, we show f_{ap} only for the RMOCKS because the statistics in the VMOCKS at these stellar masses is too low (see text). In each panel, the vertical and horizontal lines are the same as in Fig. 5.

in each mass and redshift bin. For consistency, we grouped the RMOCKS output in the same way.

In the RMOCKS and VMOCKS, the local density is computed as described in Appendix A.3, and LD and HD environments are defined as for the VIPERS sample. In the mock catalogues we do not have the absolute magnitudes in the filters needed to divide active and passive galaxies according to their location in the NUVrK plane. Instead we use their sSFR. In Fig. 3 we have shown that there is a clear difference between the distribution of the sSFR in the RMOCKS and in the data. We discussed these differences in Sect. 4.1 and Appendix C. Given these differences, we decided not to use the thresholds $\log(sSFR) < -11.2$ and $\log(sSFR) > -10.8$ (see Sect. 4.1) to define passive and active galaxies in the model, but the extremes of the sSFR distribution defined as described in Appendix C. This choice implies that f_{ap} in the model is on average in agreement with f_{ap} observed in VIPERS if we consider the entire sample regardless of environment.

We computed f_{ap} in the model in the same way as for the VIPERS sample, that is to say, we built mass-matched samples in each mass and redshift bin. To compute f_{ap}, the galaxies in the VMOCKS are weighted by using statistical weights analogous to those used in the real survey. The CSR is defined here as a smooth function ranging from 0 to 1 from $z = 0.4$ to $z = 0.6$, and it only depends on redshift. The TSR is obtained by applying SSPOC to the mock catalogues, and the SSR is mimicked by further downsampling the population as described in Sect. 2.3. In the case of the VMOCKS, as for the real data, the results are not strongly dependent on the use of these weights.

We remark that although we use the VMOCKS grouped 3 by 3, the statistics of galaxies in the highest stellar mass bin is lower in these merged mock catalogues than in the total VIPERS sample. Given the very small numbers, we did not study this stellar mass regime in the VMOCKS.

5.1. RMOCKS vs. VMOCKS

Figure 6 shows f_{ap} in the RMOCKS and VMOCKS in the same redshift and mass bins as in the data. We verified that the mass-matched samples in the mock catalogues are always in LD environments, with the exception of the highest stellar masses. The results are qualitatively similar to the results obtained with the VIPERS data set (see Sect. 5.2), with no difference between the RMOCKS and VMOCKS. This confirms that on average the VIPERS selection function does not introduce any strong bias in the measurement of f_{ap} as a function of environment.

The scatter around the mean values is larger in the VMOCKS than in the RMOCKS. This could be because of the lower number of galaxies (~40%, corresponding to the average VIPERS sampling rate), or possibly also because of the typical uncertainties in the environment reconstruction (see Sect. A.3). We also note that in the VMOCKS the dependence of f_{ap} on stellar mass in LD environments almost vanishes for $\log(\mathcal{M}_{lim}/\mathcal{M}_\odot) > 10.66$, while it is mild but evident in the RMOCKS. Finally, we do not find any dependence of f_{ap} on redshift at fixed stellar mass in either the VMOCKS or in the RMOCKS.

Given the differences between RMOCKS and VMOCKS, we expect that the trends of f_{ap} with stellar mass observed in the VIPERS sample in Fig. 5 are weaker than the true trends (especially in LD). We also expect that the difference of f_{ap} in LD and HD is less significant because of both the low(er) statistics and the errors in the environment reconstruction. Moreover, the lack of dependence of f_{ap} on redshift at fixed stellar mass that we found in the VIPERS data set does not seem to be due to the VIPERS selection function.

From now on, since we have verified that the f_{ap} behaviour is compatible in the RMOCKS and VMOCKS, we only use the RMOCKS for simplicity.

5.2. Comparison between data and RMOCKS

Figure 7 shows the VIPERS f_{ap} with f_{ap} of the RMOCKS overplotted. The trends are qualitatively similar, with f_{ap} decreasing for higher stellar masses in both LD and HD, and with f_{ap} higher in LD than in HD at all masses at $\log(\mathcal{M}/\mathcal{M}_\odot) < 11.29$. The

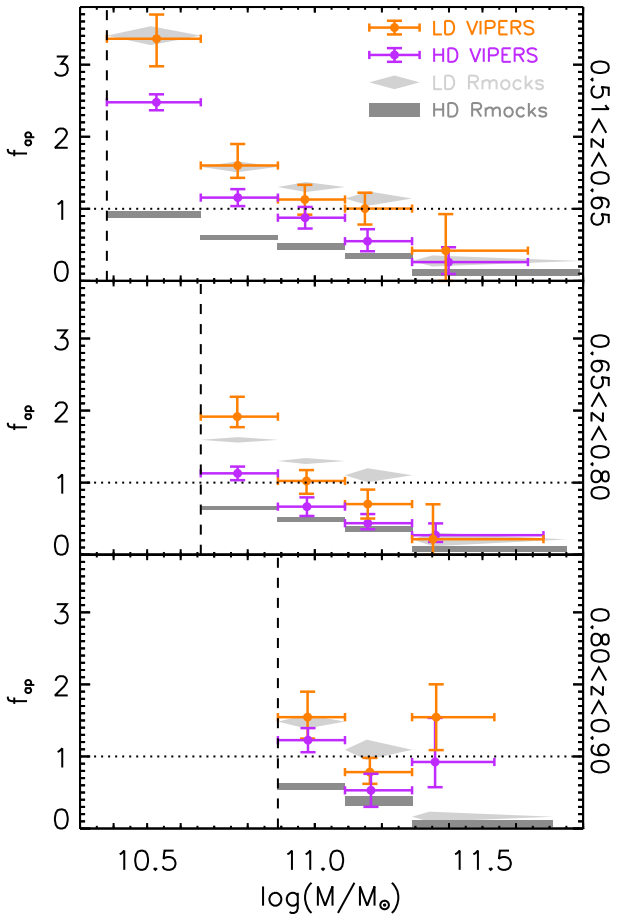

Fig. 7. Ratio of the number of active over passive galaxies (f_{ap}) in VIPERS real data (orange and violet symbols) and in the RMOCKS (filled rectangles and diamonds). The points for the RMOCKS are the same as in Fig. 6. The points for the VIPERS sample are taken from Fig. 5, but for the sake of simplicity, in each mass bin for the environment with more galaxies (LD for $\log(\mathcal{M}/\mathcal{M}_\odot) < 11.29$, HD otherwise) we plot only f_{ap} as derived from the mass-matched samples, instead of also plotting the original value as in Fig. 5.

peculiarity of f_{ap} for $\log(\mathcal{M}/\mathcal{M}_\odot) > 11.29$ at $z > 0.8$ in the data, where it does not follow the trend with stellar mass, is underlined by the fact that in the model f_{ap} is lower that in the previous mass bins.

The most remarkable result shown in Fig. 7 is that the model f_{ap} in LD environments is very similar to the one in the data, while f_{ap} in HD environments underestimates the observed f_{ap} for $\log(\mathcal{M}/\mathcal{M}_\odot) < 11.09$, and this underestimate becomes more severe as mass decreases.

6. Discussion

Unfortunately, it is not straightforward to compare different works in the field of environmental effects on galaxy evolution. Several galaxy classification systems have been adopted (by colour, SF, morphology, etc.), and the definition of environment itself can vary from analysis to analysis. Nevertheless, our results can be put into perspective by discussing the implications of our findings in the framework defined by the literature (Sect. 6.1). Moreover, our analysis with mock galaxy catalogues allows us to gain insights into the physical processes responsible for the disagreement found between our observational measurements and predictions from galaxy formation models (Sect. 6.2).

6.1. VIPERS in context

The main results of the present work are the clear preference for massive galaxies to reside in the densest environments (Fig. 4) and the fact that even at fixed stellar mass, these overdensities host a lower percentage of active galaxies than in low-density regions (Fig. 5). Although at different confidence levels, this second result seems to hold for all the stellar masses analysed in this paper up to $\log(\mathcal{M}/\mathcal{M}_\odot) = 11.29$. Above this limit we do not detect any significant dependence upon environment. We remark that these results are in qualitative agreement with the work by Malavasi et al. (2017), where we reconstruct the VIPERS large-scale filamentary structure and find that the most massive (or quiescent) galaxies are closer to filaments than less massive (or active) ones.

The stellar mass segregation that we find is expected to be a direct consequence of structure formation and hierarchical halo assembly (see Mo et al. 1997). Although some previous works, using different approaches, found the same environmental trend (e.g. Abbas & Sheth 2005; Scodeggio et al. 2009a; Wetzel et al. 2012; van der Burg et al. 2014), one recent analysis (Kafle et al. 2016) challenges this scenario by finding no evidence of stellar mass segregation in SDSS galaxy groups. Such contrasting conclusions could be explained by differences between group-finding algorithms (see Campbell et al. 2015) and/or input datasets (e.g., different proxy to recover halo masses) used by different authors. These findings again highlight the effects that different environment definitions have on the analysis of environmental effects on galaxy evolution. The debate surrounding the segregation of massive galaxies is still very much active.

In this respect, we find (Fig. 7) that at $\log(\mathcal{M}/\mathcal{M}_\odot) \gtrsim 11.3$ the SAM mocks correctly reproduce our survey, at least up to $z = 0.8$. According to the model, most of these massive galaxies are the central object in their halo, both in LD regions (>95%) and HD (>80%). Despite the mass segregation effect discussed above, their number in the LD regions is not negligible (numbers similar to those of the VIPERS sample, see Table 1). Whilst we defer a detailed study of such massive objects to a future paper in this series, here we would like to emphasise the dependence of stellar-to-halo mass ratio on the large-scale environment. This is often neglected in halo occupation distribution models (as pointed out in Tonnesen & Cen 2015). We remark that this topic, referred to as "assembly bias", is hotly debated in the literature, as shown by its long history. For instance, Lemson & Kauffmann (1999) were among the first who attempted to detect it (although they did not find it because this effect is more important for lower mass systems, which were not well resolved in earlier simulations), and it was only first measured by Gao et al. (2005) using N-body simulations.

Concerning the relative contribution of active vs. passive galaxies, we find that their ratio f_{ap} is lower in denser environments, in agreement with what has been observed in the local Universe (e.g Baldry et al. 2006) and at intermediate redshifts (e.g. DEEP2, VVDS, and zCOSMOS, see Cooper et al. 2008; Cucciati et al. 2006, 2010, respectively). These authors all used a method similar to ours, based on the n-th nearest neighbour or apertures with fixed radius, to define the local environment on comoving scales $\leqslant 5\ h^{-1}$ Mpc. Burton et al. (2013) find the same results in GAMA ($0.02 < z < 0.5$, Baldry et al. 2010) by using Voronoi tessellation and far-infrared emission as a proxy of SFR.

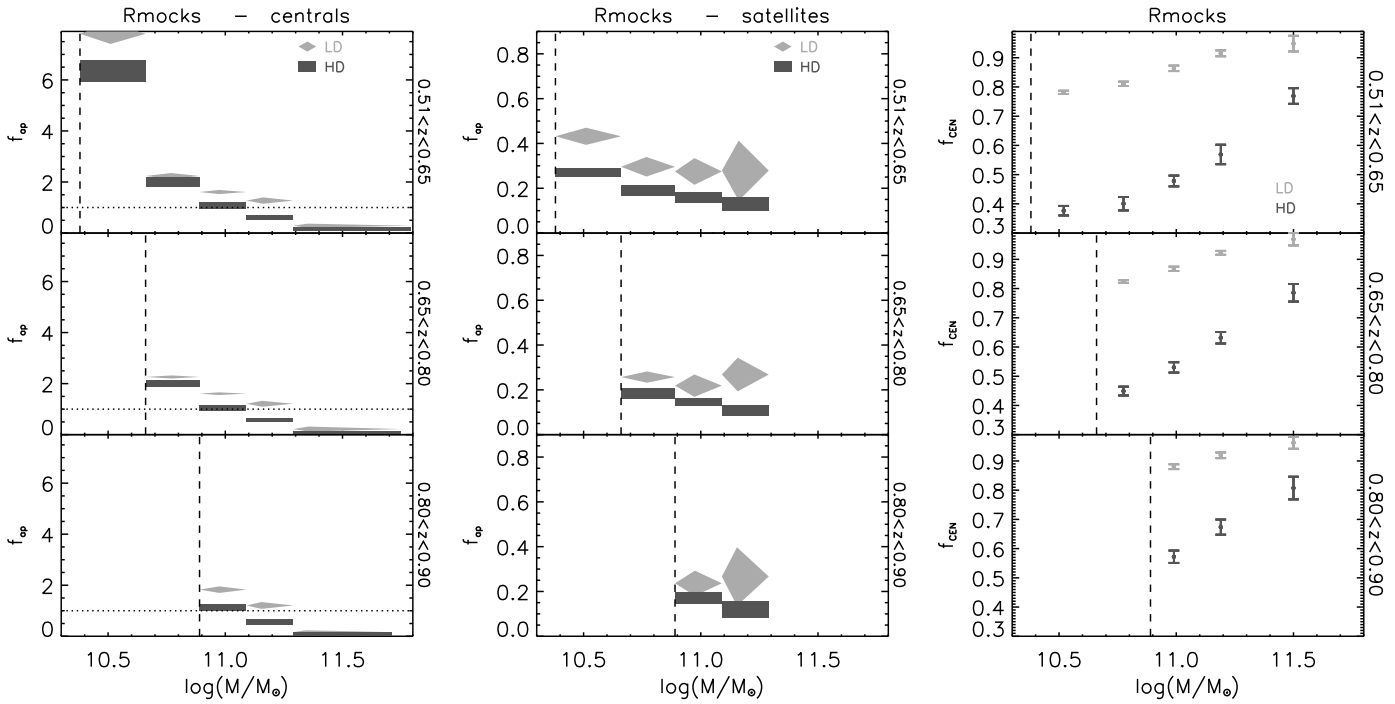

Fig. 8. *Left*: fraction f_{ap} in the RMOCKS (similar to the filled symbols in Fig. 6), but considering only central galaxies. *Middle*: as in the left panel, but considering only satellite galaxies. Note the different y-axis ranges in the *left* and *middle panels*. We plot f_{ap} only in the mass bins where there are at least 20 galaxies per light cone. *Right*: fraction of central galaxies in the RMOCKS in the same redshift ranges and stellar mass bins as in the *left* and *middle panels*. The fraction is the mean value of the 16 RMOCKS and the vertical error bar is the rms around the mean. The fraction refers to the total number of galaxies, regardless of whether they are classified passive, intermediate, or active

A similar dependence of galaxy populations on environment is observed in galaxy clusters, where the fraction of active galaxies increases as a function of cluster-centric radius (e.g. Treu et al. 2003; Raichoor & Andreon 2014; Haines et al. 2015). In agreement with our analyses, Patel et al. (2011) show that this environmental trend does not vary when different SFR estimators are used, and the decline of the SFR in groups and clusters at $0.6 < z < 0.9$ is indeed caused by a smaller fraction of active galaxies and not by a change in the global sSFR distribution.

The decrease of f_{ap} as mass increases is (qualitatively) consistent with the increase of the "red sequence fraction" adopted by Baldry et al. (2006) to analyse SDSS data. From SDSS group classification, Wetzel et al. (2012) show that such a dependence on stellar mass vanishes when only satellite galaxies are considered (although see also De Lucia et al. 2012). Similarly, as we show in Sect. 6.2, in our mock catalogues we find that satellites galaxies show a less evident dependence of f_{ap} on stellar mass than central galaxies. We have not yet attempted to identify satellites in the VIPERS sample, but if we assume that their fraction is a function of stellar mass, as our mock catalogues indicate (Fig. 8, right panel), then the observed f_{ap} should become less dependent on $\mathcal{M}$.

Several scenarios have been proposed to explain the environmental trends we observe. Quenching mechanisms like ram pressure stripping or galaxy-galaxy interactions (for an exhaustive review, see Boselli & Gavazzi 2006) are more likely to occur in overdense regions (each process in a typical environment and on typical timescales), while other processes (e.g., AGN feedback) seem to be independent of environment (at least in the VIPERS redshift range, see Rumbaugh et al. 2017). Moreover, the latter should be dominant at high masses (e.g. Peng et al. 2010; Gabor & Bournaud 2014) where indeed we find similar f_{ap} fractions in the two opposite environments.

In this respect, a missing piece of the mosaic is a precise determination of the quenching timescale, which is still debated (see e.g. the discussion in Haines et al. 2015; Moutard et al. 2016b). We address this point below, trying to reconcile the results of our mock catalogues with VIPERS. Our analysis spans over an epoch ($0.5 < z < 0.9$) when the star formation rate density (SFRD) of the Universe has already begun to decline (see Cucciati et al. 2012; Madau & Dickinson 2014), and we do see an environmental signature in galaxy quenching across the entire redshift range explored. On one hand, it is of paramount importance to understand how much environment-driven processes contribute to the SFRD decline. On the other hand, the debate is still open on the possible link between the peak of the SFRD at $z \sim 1.5$–2 and the absence, or even inversion, of the correlation between star formation activity and local density at such redshift (e.g. Mortlock et al. 2015; Alberts et al. 2016; Cucciati et al. 2006; Elbaz et al. 2007; Cooper et al. 2008; Grützbauch et al. 2011a).

6.2. Insights from the model

The remarkable agreement of f_{ap} in LD in the model and in the data and the under-prediction of f_{ap} in the model in HD suggest that a class of galaxies (e.g. the satellite galaxies, which reside mainly in HD regions, see below) with erroneous properties exists in the models, or a class with the correct properties, but with incorrect number counts.

We already know that the model by De Lucia & Blaizot (2007), similarly to most models available today, overpredicts the number of low-mass passive galaxies (e.g. Wang et al. 2007; Fontanot et al. 2009; Weinmann et al. 2010; Henriques et al. 2013; Cucciati et al. 2012). Here we show that this excess of passive galaxies is more important in high-density regions. This

was expected, to some extent, because such low-mass passive galaxies are preferentially satellites (also see below), which reside in the high-density regions given by galaxy groups and clusters. In the models, galaxies undergo some physically motivated processes when they become satellites. These have the net effect of quenching the SF. It has been pointed out in the literature that these processes are probably modelled to be too strong or too quick, causing an overprediction of relatively low-mass passive galaxies. Some more recent models have tried to mitigate this quenching (e.g. Font et al. 2008; Guo et al. 2010), and also obtained improvements on the environmental effects on galaxy star formation (e.g. Henriques et al. 2016). However, the excess of low-mass passive galaxies might not just be a problem resulting from over-efficient hot-gas stripping when a galaxy becomes a satellite. For instance, Hirschmann et al. (2016) show that this excess can be significantly reduced by modifying the stellar feedback scheme (i.e. in this case, the properties of galaxies change at the time they become satellites), and argue that the quenching timescales are not primarily determined by environmental processes.

We can verify whether the low f_{ap} values in HD in the RMOCKS are mainly due to the satellite galaxies by separating them from the central galaxies. In Fig. 8 we show f_{ap} in the RMOCKS using only central (left panel) or only satellite galaxies (middle panel). We find the following:

- f_{ap} is much higher for central galaxies than for satellites for all stellar masses, environments, and redshift ranges. This is especially true for $\log(\mathcal{M}/\mathcal{M}_\odot) < 11.09$.
- f_{ap} is higher in LD than HD environments, at all masses below $\log(\mathcal{M}/\mathcal{M}_\odot) = 11.29$ for both centrals and satellites.
- f_{ap} in HD increases for lower stellar masses for both central and satellite galaxies, but this increase is much steeper for centrals than for satellites.
- f_{ap} in LD shows the same increase as in HD at lower stellar masses for central galaxies, while for satellite galaxies it seems to depend very weakly (if at all) on stellar mass, at least for $\log(\mathcal{M}/\mathcal{M}_\odot) > 10.66$.
- In HD, f_{ap} is always higher for central galaxies than for the total sample (see Fig. 6), while for satellite galaxies it is always lower than for the total sample. Moreover, in HD the increase of f_{ap} for the central galaxies towards lower masses is much steeper than that of the total sample.

The low f_{ap} in HD in the total sample at the lowest masses is clearly due to the satellite galaxies. The SF is much more quenched in satellite than in the central galaxies, and they are more abundant in HD at these masses (see the rightmost panel of Fig. 8). In contrast, in LD environments the total sample is dominated by central galaxies.

The very low fraction of active galaxies in HD in the model with respect to the real data could be due to an excessive quenching of satellite galaxies or to an excessive number of satellite galaxies. In contrast, it seems that in LD the model is able to reproduce the correct balance of satellite and central, and their respective quenching, in order to agree with the data. This result is helpful for improving the inclusion of environment-driven processes in the model. However, for a more meaningful comparison it would be necessary to identify central and satellite galaxies in the real data as well, which is not an easy task (although see e.g. Kovač et al. 2014, for a central-satellite classification at $z \sim 0.7$); we defer this analysis of the VIPERS sample to future work.

It is not the aim of this work to perform a detailed analysis of the environmental history of galaxies in the model. However, we

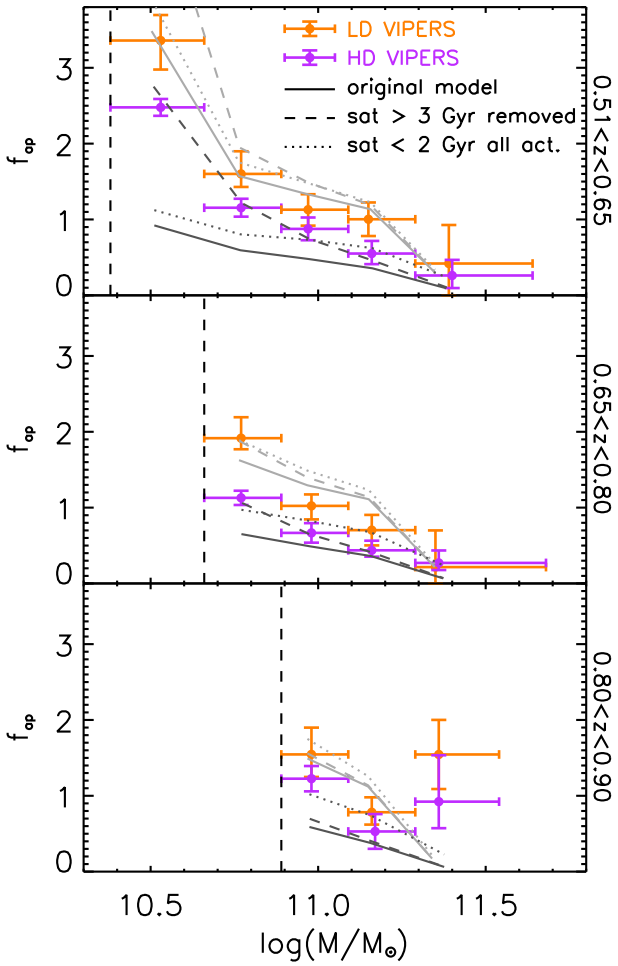

Fig. 9. Fraction f_{ap} in the VIPERS data (orange and violet crosses) and in the model (grey lines). Crosses are the same as in Fig. 7. Solid grey lines refer to RMOCKS and correspond to the grey polygons of Fig. 6. Dashed lines refer to RMOCKS, but are computed after removing satellite galaxies that became satellites more than 3 Gyr before. The dotted lines refer to RMOCKS, but are computed considering all the "young" satellite galaxies (i.e., that became satellites less than 2 Gyr before) to be active. See the text for more details.

performed a simple test to verify two hypotheses. We assumed that there are too many low-mass passive satellites in the simulation because either i) they survived (when they should not have) the disruption of multiple mergers or encounters; or ii) they are already passive (when they should not be) because the quenching mechanisms are too fast or strong. In the first case we investigate the total number of satellites in the model, in the second case we investigate their star formation activity.

We address these two possibilities in the following way. We study the merger tree of the satellite galaxies, and we find the time t_{sat} at which they became satellites. The time t_{sat} is defined as the last time when the main progenitor of the satellite galaxy is a central galaxy. As a first check, we verified that at all stellar masses and redshifts explored, galaxies in HD became satellites on average 0.5–1 Gyr before galaxies in LD environments. Secondly, we recomputed f_{ap} in the RMOCKS by modifying the sample of satellite galaxies in two ways: i) we removed all the galaxies that became satellites more than X Gyr before the time of observation from the sample, to take into account the fact that some of them should have been destroyed); ii) we considered all the passive satellites that became satellites less than Y Gyr before to be active, to compensate for the possibility that the quenching

they have undergone at the moment of becoming satellites was too strong or quick.

We explored different values of X and Y. In Fig. 9 we show f_{ap} in the RMOCKS for $X = 3$ Gyr and $Y = 2$ Gyr, that is to say, the values for which in HD the model f_{ap} is more similar to the data f_{ap}. We remark that to keep this toy model as simple as possible, we used the same X and Y at all stellar masses and at all redshifts, and in both environments.

In the first case (the removal of satellites), the model f_{ap} in HD is in agreement with observations when we exclude galaxies that became satellites more than 3 Gyr before from the sample. This is true at all masses in the redshift range $0.51 < z < 0.8$, but at $z > 0.8$ we would need to remove even more "recent" satellites ($X < 3$ Gyr) to make the model f_{ap} agree with the observed f_{ap} (we would need to remove all the galaxies that became satellites more than 1 Gyr before). Figure 9 also shows that by removing such satellites regardless of their environment, we also increase f_{ap} in LD (especially at the lowest redshift), which now would over-predict the observed one. We note that the fraction of removed satellites is non-negligible and strongly depends on stellar mass. In the lowest redshift bin, in HD it ranges from ∼50% to ∼30% going from the lowest to the highest stellar masses. These fractions become smaller and smaller at higher redshift. These trends, together with the fact that the satellite fraction is higher at lower masses, explain why f_{ap} changes much more at low masses and at low redshift. Moreover, they are smaller in LD at all redshifts, but still non-negligible at $0.51 < z < 0.65$, where we remove ∼40% of the satellites with the lowest masses, so that f_{ap} also increases in LD in this redshift and mass regime.

In contrast, by moving satellites from the passive to the active population, for $Y = 2$ Gyr the model f_{ap} in HD is in better agreement with the observed one at $z > 0.65$, while at $z < 0.65$ f_{ap} in HD is still too low for $\log(\mathcal{M}/\mathcal{M}_\odot) < 10.89$. It is possible to increase f_{ap} at low masses by increasing Y, but in this way f_{ap} in HD would become too high at higher stellar masses, and at all masses at higher redshift (we refer e.g. to Wetzel et al. 2012; and Hirschmann et al. 2014, for a discussion of the mass dependence of the quenching timescales). For $Y = 2$ Gyr, the fraction of passive satellites that we move into the star-forming population increases with increasing stellar mass and (mildly) with increasing redshift. Moreover, it is similar in HD and LD. For instance, it ranges from ∼15% to ∼45% from the lowest to the highest stellar masses in the lowest redshift bin. Given that we move a larger satellite fraction at higher masses, but the overall satellite contribution (right panel of Fig. 8) increases for lower masses, the net effect is that f_{ap} increases roughly homogeneously at all stellar masses.

In conclusion, both these changes to the model significantly increase the agreement between the model and the data, even if neither of them is able to reproduce the data over the entire range of stellar mass, environment, and redshift. Clearly, by considering the two cases separately, we make an over-simplistic assumption. It is probable that the problem is (at the very least) two-fold: the model has too many low-mass satellites, and too many of them (even of the "right" ones) have been too heavily quenched. Moreover, these effects are likely to depend in different ways on redshift, stellar mass, and environment. In summary, this simple test tells us that in order to fine-tune a model of galaxy formation, we need to provide solid observational constraints considering the local environment of galaxies, possibly in a broad redshift range to better model the quenching timescales, which is not an easy task.

7. Summary and conclusions

VIPERS is a flux-limited survey ($i < 22.5$) conceived to be an analogue of the local 2dFDRS, but at higher redshift ($0.5 < z < 1.2$). Thanks to the large volume explored, we can study galaxy evolution with accurate statistics and also perform detailed analyses of rare galaxy populations, such as the most massive galaxies. In this work, we used the final VIPERS release to study how environment affects the sSFR in galaxies. We defined the environment as the galaxy density contrast computed using cylindrical top-hat filters, on scales corresponding to the fifth nearest neighbour, by using spectroscopic redshifts and additionally photometric redshifts for the galaxies without reliable spectroscopic measurements. We verified the reliability of the density field reconstruction using galaxy mock catalogues mimicking the VIPERS observational strategy. The main results of our analysis are as follows:

- More massive galaxies tend to reside in high-density regions (HD) rather than in low-density regions (LD). This is true throughout the entire explored redshift range ($0.51 < z < 0.9$), in agreement with previous works.
- We defined active and passive galaxies by means of the (NUV$-r$) vs. ($r - K$) colour-colour diagram, and we studied how the fraction f_{ap} of active over passive galaxies depends on environment at fixed stellar mass. We found that f_{ap} is higher in LD than in HD, from the lowest stellar masses explored ($\log(\mathcal{M}/\mathcal{M}_\odot) = 10.38$) at least up to $\log(\mathcal{M}/\mathcal{M}_\odot) \sim 11.3$, although with decreasing significance from lower to higher masses.
- We performed the same analysis on VIPERS-like mock galaxy catalogues, based on the model of galaxy formation and evolution by De Lucia & Blaizot (2007). We found that the model f_{ap} reproduces the observed f_{ap} in LD VIPERS environments well, but it underpredicts f_{ap} in HD environments. This is especially the case for the lowest stellar masses. We verified that this underprediction is mainly due to an excess of low-mass passive satellite galaxies in the model.
- By studying the time t_{sat} when galaxies became satellites, we verified that f_{ap} in the model could become too low in two different ways: (i) through the spurious presence of "old" satellites that are still present in the simulation more than 3 Gyr after t_{sat}, which should have been disrupted by close encounters; (ii) by too rapid or strong quenching processes in "young" satellites that terminate star formation in galaxies that have recently (<2 Gyr) become satellites.

Our results are in very good agreement with other works performed with the VIPERS sample, that is, with the study of the galaxy stellar mass function per environment (Davidzon et al. 2016, based on a previous VIPERS release) and the study of galaxy properties with relation to distance from filaments describing the VIPERS large-scale structure (Malavasi et al. 2017, based on the same VIPERS release as this work, but with a different definition of environment).

It is difficult to perform a quantitative comparison of our results with similar works in the literature because of the different environment definitions (or the same definition, but different tracer samples) and the different galaxy-type classification. Nevertheless, this is the first time that environmental effects on high-mass galaxies are clearly seen up to $z \sim 0.9$. This result throws doubts on the hypothesis that stellar mass is the only driver of SF quenching in galaxies with $\log(\mathcal{M}/\mathcal{M}_\odot) \gtrsim 10.6$ (see e.g. Peng et al. 2010).

Our study extends up to $z \sim 0.9$, and we find an environmental signature in galaxy quenching across the entire redshift range (although less clear at $0.8 < z < 0.9$ because of the lower mass range probed). This is an epoch at which the star formation rate density (SFRD) of the Universe has begun to decline. It is of paramount importance to understand the reasons for this decline and to which extent environment-driven processes contribute to it. In this respect, solid environmental studies at $z \lesssim 1$–1.5 could give important clues to define this picture. Needless to say, we also need a continuous feedback between observations and models of galaxy formation and evolution. Our comparison with the model proposed by De Lucia & Blaizot and our simple toy model based on the time when galaxies became satellites suggests that we need to provide solid observational constraints also based on galaxy local environment, possibly in a broad redshift range to better model quenching timescales. We need a combined effort to develop in parallel more efficient instruments and surveys to study the local galaxy environment at high redshift (for an example of what can be done in this regard with Euclid, see e.g. Cucciati et al. 2016) and better fine-tuned models to understand how and at which pace galaxies evolve through the cosmic large-scale structure of the Universe.

Acknowledgements. We acknowledge the crucial contribution of the ESO staff for the management of service observations. In particular, we are deeply grateful to M. Hilker for his constant help and support of this program. We thank the anonymous referee for the useful comments and suggestions. Italian participation to VIPERS has been funded by INAF through PRIN 2008, 2010, and 2014 programs. L.G., A.J.H., and B.R.G. acknowledge support from the European Research Council through grant No. 291521. O.L.F. acknowledges support from the European Research Council through grant No. 268107. J.A.P. acknowledges support of the European Research Council through grant No. 67093. R.T. acknowledges financial support from the European Research Council through grant no. 202686. A.P., K.M., and J.K. have been supported by the National Science Centre (grants UMO-2012/07/B/ST9/04425 and UMO-2013/09/D/ST9/04030). W.J.P. is also grateful for support from the UK Science and Technology Facilities Council through the grant ST/I001204/1. E.B., F.M. and L.M. acknowledge the support from grants ASI-INAF I/023/12/0 and PRIN MIUR 2010–2011. L.M. also acknowledges financial support from PRIN INAF 2012. S.D.L.T. and M.P. acknowledge the support of the OCEVU Labex (ANR-11-LABX-0060) and the A*MIDEX project (ANR-11-IDEX-0001-02) funded by the "Investissements d'Avenir" French government program managed by the ANR and the Programme National Galaxies et Cosmologie (PNCG). T.M. and S.A. acknowledge financial support from the ANR Spin(e) through the french grant ANR-13-BS05-0005. Research conducted within the scope of the HECOLS International Associated Laboratory, supported in part by the Polish NCN grant DEC-2013/08/M/ST9/00664.

References

Abbas, U., & Sheth, R. K. 2005, MNRAS, 364, 1327
Alberts, S., Pope, A., Brodwin, M., et al. 2016, ApJ, 825, 72
Alpaslan, M., Robotham, A. S. G., Obreschkow, D., et al. 2014, MNRAS, 440, L106
Annunziatella, M., Biviano, A., Mercurio, A., et al. 2014, A&A, 571, A80
Arnouts, S., Le Floc'h, E., Chevallard, J., et al. 2013, A&A, 558, A67
Baldry, I. K., Balogh, M. L., Bower, R. G., et al. 2006, MNRAS, 373, 469
Baldry, I. K., Robotham, A. S. G., Hill, D. T., et al. 2010, MNRAS, 404, 86
Balogh, M. L., Schade, D., Morris, S. L., et al. 1998, ApJ, 504, L75
Boselli, A., & Gavazzi, G. 2006, PASP, 118, 517
Boselli, A., Voyer, E., Boissier, S., et al. 2014, A&A, 570, A69
Bottini, D., Garilli, B., Maccagni, D., et al. 2005, PASP, 117, 996
Boylan-Kolchin, M., Springel, V., White, S. D. M., Jenkins, A., & Lemson, G. 2009, MNRAS, 398, 1150
Bruzual, G., & Charlot, S. 2003, MNRAS, 344, 1000
Burton, C. S., Jarvis, M. J., Smith, D. J. B., et al. 2013, MNRAS, 433, 771
Calzetti, D., Armus, L., Bohlin, R. C., et al. 2000, ApJ, 533, 682
Campbell, D., van den Bosch, F. C., Hearin, A., et al. 2015, MNRAS, 452, 444
Cen, R. 2011, ApJ, 741, 99
Chevallard, J., Charlot, S., Wandelt, B., & Wild, V. 2013, MNRAS, 432, 2061
Colless, M., Dalton, G., Maddox, S., et al. 2001, MNRAS, 328, 1039
Conroy, C., Gunn, J. E., & White, M. 2009, ApJ, 699, 486
Cooper, M., Newman, J., Madgwick, D., et al. 2005, ApJ, 634, 833
Cooper, M. C., Newman, J. A., Coil, A. L., et al. 2007, MNRAS, 376, 1445
Cooper, M. C., Newman, J. A., Weiner, B. J., et al. 2008, MNRAS, 383, 1058
Cucciati, O., Iovino, A., Marinoni, C., et al. 2006, A&A, 458, 39
Cucciati, O., Marinoni, C., Iovino, A., et al. 2010, A&A, 520, A42
Cucciati, O., Tresse, L., Ilbert, O., et al. 2012, A&A, 539, A31
Cucciati, O., Granett, B. R., Branchini, E., et al. 2014, A&A, 565, A67
Cucciati, O., Marulli, F., Cimatti, A., et al. 2016, MNRAS, 462, 1786
Darvish, B., Mobasher, B., Sobral, D., Scoville, N., & Aragon-Calvo, M. 2015, ApJ, 805, 121
Davidzon, I., Bolzonella, M., Coupon, J., et al. 2013, A&A, 558, A23
Davidzon, I., Cucciati, O., Bolzonella, M., et al. 2016, A&A, 586, A23
Davis, M., & Geller, M. J. 1976, ApJ, 208, 13
de la Torre, S., Guzzo, L., Kovač, K., et al. 2010, MNRAS, 409, 867
de la Torre, S., Guzzo, L., Peacock, J. A., et al. 2013, A&A, 557, A54
De Lucia, G., & Blaizot, J. 2007, MNRAS, 375, 2
De Lucia, G., Weinmann, S., Poggianti, B. M., Aragón-Salamanca, A., & Zaritsky, D. 2012, MNRAS, 423, 1277
De Lucia, G., Tornatore, L., Frenk, C. S., et al. 2014, MNRAS, 445, 970
Dressler, A. 1980, ApJ, 236, 351
Einasto, M., Lietzen, H., Tempel, E., et al. 2014, A&A, 562, A87
Elbaz, D., Daddi, E., Le Borgne, D., et al. 2007, A&A, 468, 33
Emerson, J. P., Sutherland, W. J., McPherson, A. M., et al. 2004, The Messenger, 117, 27
Font, A. S., Bower, R. G., McCarthy, I. G., et al. 2008, MNRAS, 389, 1619
Fontanot, F., De Lucia, G., Monaco, P., Somerville, R. S., & Santini, P. 2009, MNRAS, 397, 1776
Fossati, M., Wilman, D. J., Fontanot, F., et al. 2015, MNRAS, 446, 2582
Fossati, M., Wilman, D. J., Mendel, J. T., et al. 2017, ApJ, 835, 153
Fritz, A., Scodeggio, M., Ilbert, O., et al. 2014, A&A, 563, A92
Fukugita, M., Ichikawa, T., Gunn, J. E., et al. 1996, AJ, 111, 1748
Gabor, J. M., & Bournaud, F. 2014, MNRAS, 441, 1615
Gabor, J. M., Davé, R., Finlator, K., & Oppenheimer, B. D. 2010, MNRAS, 407, 749
Gao, L., Springel, V., & White, S. D. M. 2005, MNRAS, 363, L66
Garilli, B., Paioro, L., Scodeggio, M., et al. 2012, PASP, 124, 1232
Gavazzi, G., Fumagalli, M., Cucciati, O., & Boselli, A. 2010, A&A, 517, A73
Gehrels, N. 1986, ApJ, 303, 336
Gerke, B. F., Newman, J. A., Davis, M., et al. 2012, ApJ, 751, 50
Gómez, P., Nichol, R., Miller, C., et al. 2003, ApJ, 584, 210
Grützbauch, R., Chuter, R. W., Conselice, C. J., et al. 2011a, MNRAS, 412, 2361
Grützbauch, R., Conselice, C. J., Bauer, A. E., et al. 2011b, MNRAS, 418, 938
Guo, Q., White, S., Li, C., & Boylan-Kolchin, M. 2010, MNRAS, 404, 1111
Guo, Q., White, S., Boylan-Kolchin, M., et al. 2011, MNRAS, 413, 101
Guo, Q., White, S., Angulo, R. E., et al. 2013, MNRAS, 428, 1351
Guzzo, L., Scodeggio, M., Garilli, B., et al. 2014, A&A, 566, A108
Haas, M. R., Schaye, J., & Jeeson-Daniel, A. 2012, MNRAS, 419, 2133
Haines, C. P., Pereira, M. J., Smith, G. P., et al. 2015, ApJ, 806, 101
Hashimoto, Y., Oemler, Jr., A., Lin, H., & Tucker, D. L. 1998, ApJ, 499, 589
Hawken, A. J., Granett, B. R., Iovino, A., et al. 2017, A&A, accepted
Henriques, B. M. B., White, S. D. M., Thomas, P. A., et al. 2013, MNRAS, 431, 3373
Henriques, B. M. B., White, S. D. M., Thomas, P. A., et al. 2015, MNRAS, 451, 2663
Henriques, B. M. B., White, S. D. M., Thomas, P. A., et al. 2016, MNRAS, submitted [arXiv:1611.02286]
Hinshaw, G., Larson, D., Komatsu, E., et al. 2013, ApJS, 208, 19
Hirschmann, M., De Lucia, G., Wilman, D., et al. 2014, MNRAS, 444, 2938
Hirschmann, M., De Lucia, G., & Fontanot, F. 2016, MNRAS, 461, 1760
Ilbert, O., Tresse, L., Zucca, E., et al. 2005, A&A, 439, 863
Ilbert, O., Capak, P., Salvato, M., et al. 2009, ApJ, 690, 1236
Ilbert, O., McCracken, H. J., Le Fèvre, O., et al. 2013, A&A, 556, A55
Iovino, A., Cucciati, O., Scodeggio, M., et al. 2010, A&A, 509, A40
Iovino, A., Petropoulou, V., Scodeggio, M., et al. 2016, A&A, 592, A78
Jarvis, M. J., Bonfield, D. G., Bruce, V. A., et al. 2013, MNRAS, 428, 1281
Kafle, P. R., Robotham, A. S. G., Lagos, C. D. P., et al. 2016, MNRAS, 463, 4194
Kaiser, N. 1987, MNRAS, 227, 1
Kauffmann, G., White, S. D. M., Heckman, T. M., et al. 2004, MNRAS, 353, 713
Klypin, A. A., Trujillo-Gomez, S., & Primack, J. 2011, ApJ, 740, 102
Knobel, C., Lilly, S. J., Kovač, K., et al. 2013, ApJ, 769, 24
Komatsu, E., Smith, K. M., Dunkley, J., et al. 2011, ApJS, 192, 18
Kovač, K., Lilly, S. J., Cucciati, O., et al. 2010, ApJ, 708, 505
Kovač, K., Lilly, S. J., Knobel, C., et al. 2014, MNRAS, 438, 717

Le Fèvre, O., Mancini, D., Saisse, M., et al. 2002, The Messenger, 109, 21
Le Fèvre, O., Saisse, M., Mancini, D., et al. 2003, in Instrument Design and Performance for Optical/Infrared Ground-based Telescopes, eds. M. Iye, A. F. M. Moorwood, Proc. SPIE, 4841, 1670
Le Fèvre, O., Vettolani, G., Garilli, B., et al. 2005, A&A, 439, 845
Lemaux, B. C., Tomczak, A. R., Lubin, L. M., et al. 2016, MNRAS, submitted [arXiv:1608.00973]
Lemson, G., & Kauffmann, G. 1999, MNRAS, 302, 111
Lilly, S. J., Le Brun, V., Maier, C., et al. 2009, ApJS, 184, 218
Madau, P., & Dickinson, M. 2014, ARA&A, 52, 415
Malavasi, N., Pozzetti, L., Cucciati, O., Bardelli, S., & Cimatti, A. 2016, A&A, 585, A116
Malavasi, N., Arnouts, S., Vibert, D., et al. 2017, MNRAS, 465, 3817
Marinoni, C., Davis, M., Newman, J. A., & Coil, A. L. 2002, ApJ, 580, 122
Martin, C., & GALEX Team. 2005, in Maps of the Cosmos, eds. M. Colless, L. Staveley-Smith, & R. A. Stathakis, IAU Symp., 216, 221
Marulli, F., Bolzonella, M., Branchini, E., et al. 2013, A&A, 557, A17
Mellier, Y., Bertin, E., Hudelot, P., et al. 2008, http://terapix.iap.fr/cplt/oldSite/Descart/CFHTLS-T0005-Release.pdf
Micheletti, D., Iovino, A., Hawken, A. J., et al. 2014, A&A, 570, A106
Mo, H. J., Jing, Y. P., & White, S. D. M. 1997, MNRAS, 284, 189
Moresco, M., Pozzetti, L., Cimatti, A., et al. 2013, A&A, 558, A61
Mortlock, A., Conselice, C. J., Hartley, W. G., et al. 2015, MNRAS, 447, 2
Moutard, T., Arnouts, S., Ilbert, O., et al. 2016a, A&A, 590, A102
Moutard, T., Arnouts, S., Ilbert, O., et al. 2016b, A&A, 590, A103
Muldrew, S. I., Croton, D. J., Skibba, R. A., et al. 2012, MNRAS, 419, 2670
Oemler, A. 1974, ApJ, 194, 1
Oke, J. B. 1974, ApJS, 27, 21
Patel, S. G., Kelson, D. D., Holden, B. P., Franx, M., & Illingworth, G. D. 2011, ApJ, 735, 53
Peng, Y.-j., Lilly, S. J., Kovač, K., et al. 2010, ApJ, 721, 193
Pozzetti, L., Bolzonella, M., Zucca, E., et al. 2010, A&A, 523, A13
Prada, F., Klypin, A. A., Cuesta, A. J., Betancort-Rijo, J. E., & Primack, J. 2012, MNRAS, 423, 3018
Prevot, M. L., Lequeux, J., Prevot, L., Maurice, E., & Rocca-Volmerange, B. 1984, A&A, 132, 389
Puget, P., Stadler, E., Doyon, R., et al. 2004, in Ground-based Instrumentation for Astronomy, eds. A. F. M. Moorwood, & M. Iye, Proc. SPIE, 5492, 978
Raichoor, A., & Andreon, S. 2014, A&A, 570, A123
Rumbaugh, N., Lemaux, B. C., Tomczak, A., et al. 2017, MNRAS, 466, 496
Schaye, J., Crain, R. A., Bower, R. G., et al. 2015, MNRAS, 446, 521
Scodeggio, M., Franzetti, P., Garilli, B., Le Fèvre, O., & Guzzo, L. 2009a, The Messenger, 135, 13
Scodeggio, M., Vergani, D., Cucciati, O., et al. 2009b, A&A, 501, 21
Scodeggio, M., Guzzo, L., Garilli, B., et al. 2017, A&A, in press, DOI: 10.1051/0004-6361/201630114
Scoville, N., Arnouts, S., Aussel, H., et al. 2013, ApJ, 206, 3
Speagle, J. S., Steinhardt, C. L., Capak, P. L., & Silverman, J. D. 2014, ApJS, 214, 15
Spergel, D. N., Verde, L., Peiris, H. V., et al. 2003, ApJS, 148, 175
Springel, V., White, S. D. M., Jenkins, A., et al. 2005, Nature, 435, 629
Tempel, E., Stoica, R. S., & Saar, E. 2013, MNRAS, 428, 1827
Tonnesen, S., & Cen, R. 2015, ApJ, 812, 104
Treu, T., Ellis, R. S., Kneib, J.-P., et al. 2003, ApJ, 591, 53
van der Burg, R. F. J., Muzzin, A., Hoekstra, H., et al. 2014, A&A, 561, A79
Vogelsberger, M., Genel, S., Springel, V., et al. 2014, MNRAS, 444, 1518
Wang, L., Li, C., Kauffmann, G., & De Lucia, G. 2007, MNRAS, 377, 1419
Weinmann, S. M., Kauffmann, G., von der Linden, A., & De Lucia, G. 2010, MNRAS, 406, 2249
Wetzel, A. R., Tinker, J. L., & Conroy, C. 2012, MNRAS, 424, 232
Whitaker, K. E., Franx, M., Leja, J., et al. 2014, ApJ, 795, 104
Zucca, E., Bardelli, S., Bolzonella, M., et al. 2009, A&A, 508, 1217

[1] INAF–Osservatorio Astronomico di Bologna, via Ranzani 1, 40127 Bologna, Italy
[2] Dipartimento di Fisica e Astronomia – Alma Mater Studiorum Università di Bologna, viale Berti Pichat 6/2, 40127 Bologna, Italy
[3] Aix Marseille Univ, CNRS, LAM, Laboratoire d'Astrophysique de Marseille, 13013 Marseille, France
[4] INAF–Osservatorio Astronomico di Brera, via Brera 28, 20122 Milano – via E. Bianchi 46, 23807 Merate, Italy
[5] Università degli Studi di Milano, via G. Celoria 16, 20133 Milano, Italy
[6] INAF–Osservatorio Astronomico di Trieste, via G. B. Tiepolo 11, 34143 Trieste, Italy
[7] Dipartimento di Matematica e Fisica, Università degli Studi Roma Tre, via della Vasca Navale 84, 00146 Roma, Italy
[8] INFN, Sezione di Roma Tre, via della Vasca Navale 84, 00146 Roma, Italy
[9] INAF–Osservatorio Astronomico di Roma, via Frascati 33, 00040 Monte Porzio Catone (RM), Italy
[10] INAF–Istituto di Astrofisica Spaziale e Fisica Cosmica Milano, via Bassini 15, 20133 Milano, Italy
[11] INAF–Osservatorio Astrofisico di Torino, 10025 Pino Torinese, Italy
[12] Laboratoire Lagrange, UMR7293, Université de Nice Sophia Antipolis, CNRS, Observatoire de la Côte d'Azur, 06300 Nice, France
[13] Institute of Physics, Jan Kochanowski University, ul. Swietokrzyska 15, 25-406 Kielce, Poland
[14] National Centre for Nuclear Research, ul. Hoza 69, 00-681 Warszawa, Poland
[15] INFN, Sezione di Bologna, viale Berti Pichat 6/2, 40127 Bologna, Italy
[16] Department of Astronomy & Physics, Saint Mary's University, 923 Robie Street, Halifax, Nova Scotia, B3H 3C3, Canada
[17] Aix-Marseille Universite, Jardin du Pharo, 58 bd Charles Livon, 13284 Marseille Cedex 7, France
[18] IRAP, 9 Av. du Colonel Roche, BP 44346, 31028 Toulouse Cedex 4, France
[19] Astronomical Observatory of the Jagiellonian University, Orla 171, 30-001 Cracow, Poland
[20] School of Physics and Astronomy, University of St Andrews, St. Andrews KY16 9SS, UK
[21] INAF–Istituto di Astrofisica Spaziale e Fisica Cosmica Bologna, via Gobetti 101, 40129 Bologna, Italy
[22] INAF–Istituto di Radioastronomia, via Gobetti 101, 40129 Bologna, Italy
[23] Aix Marseille Univ., Univ. Toulon, CNRS, CPT, 13284 Marseille, France
[24] Univ. Lyon, Univ. Lyon1, ENS de Lyon, CNRS, Centre de Recherche Astrophysique de Lyon, UMR 5574, 69230 Saint-Genis-Laval, France
[25] Department of Astronomy, University of Geneva, Ch. d'Ecogia 16, 1290 Versoix, Switzerland
[26] Institute for Astronomy, University of Edinburgh, Royal Observatory, Blackford Hill, Edinburgh EH9 3HJ, UK

Appendix A: Density field reconstruction

We summarise the procedure used to derive the VIPERS density field and to assess the reliability of its computation.

A.1. Local density ρ

Several factors need to be taken into account when computing the local density $\rho(\boldsymbol{r})$ (Eq. (2)) and its mean value $\langle\rho(\boldsymbol{r}(z))\rangle$. A detailed description of the procedure and its parameters are described in Kovač et al. (2010). Here we discuss the most relevant issues that we considered for our analysis.

1) Tracer galaxies. We used both flux-limited tracers ($i \leq 22.5$) and volume-limited tracers. For the latter, we imposed three different luminosity limits given by $M_B \leq M_{\rm lim} - Qz$ and $M_{\rm lim} = -19.9, -20.4$, and -20.9 to define tracer samples complete down to $z = 0.8, 0.9$, and 1.0, respectively. We used $Q = 1$ to account for the evolution of the characteristic luminosity of the galaxy luminosity function (see e.g. Zucca et al. 2009; and Kovač et al. 2010). By using the flux-limited tracers, ρ can be computed on much smaller scales than with volume-limited tracers (which are sparser by definition). In contrast, by using the volume-limited tracers, we can compute ρ with the same tracer population at all redshifts.

2) Smoothing filter. For the VIPERS sample, we computed ρ with different smoothing filters: i) cylinders with a half-length of $1000\,{\rm km\,s^{-1}}$ and radius corresponding to the distance to the fifth, tenth, and twentieth n.n. (we call these radii $R_{\rm 5th}$, $R_{\rm 10th}$, and $R_{\rm 20th}$); ii) cylinders with a half-length of $1000\,{\rm km\,s^{-1}}$ and radius $R = 2, 3, 4, 5$, and $8\,h^{-1}$ Mpc (radii $R_{\rm 2c}$, $R_{\rm 3c}$, $R_{\rm 4c}$, $R_{\rm 5c}$, and $R_{\rm 8c}$); and iii) spheres with radius $R = 5$ and $8\,h^{-1}$ Mpc as done in Cucciati et al. (2014) (radii $R_{\rm 5s}$ and $R_{\rm 8s}$). A fixed-scale R allows us to study the entire range of local densities on the same scale. In contrast, when we use an adaptive R, we are able to reach much smaller scales in high-density regions (but larger scales in low-density regions). A cylindrical filter, being elongated along the line of sight, is better suited for redshift space, like in our case: in this way, we can better account for the peculiar velocities of galaxies in high densities while keeping a relatively small scale on the plane of the sky. In the case of cylinders, the radius R is computed in the RA-Dec plane from the cylinder centre, and for the adaptive radius the nth n.n. is computed in 2D on the plane of the sky, considering all galaxies within $\pm 1000\,{\rm km\,s^{-1}}$ to be at the same redshift. For all the tracers within the filter, we set $F(R) = 1/(\pi R^2)$, and $\rho(\boldsymbol{r})$ has the dimensions of a surface density. For the spherical filter, tracer counts are made in 3D comoving space within a sphere of radius R, and we set $F(R) = 1/(4/3\pi R^3)$. In this case, $\rho(\boldsymbol{r})$ has the dimensions of a volume density.

3) Cell position. The aim of this work is to study how the local environment around galaxies affects their evolution, therefore we centred the cells on our galaxies. Tracer galaxies at the centre of a smoothing element are included in the count.

4) Weights. The function ϕ in Eq. (2) normally takes into account the survey selection function. In the case of VIPERS, ϕ should include the weights CSR, TSR, and SSR discussed in Sect. 2.1. Alternatively, we can use $\phi = 1$ for our spectroscopic sample, but we also include in the tracer sample the galaxies for which we only have a photometric redshift. In this way, our tracer sample will be complete in the studied volume. We followed this second approach, and we minimised the effects of the large photometric redshift error by modifying the PDF of $z_{\rm p}$ using the "ZADE" method (see Appendix A.2). We refer to Cucciati et al. (2014) for a detailed comparison of the two approaches. Briefly, the ZADE method allows us a density reconstruction with much smaller random errors.

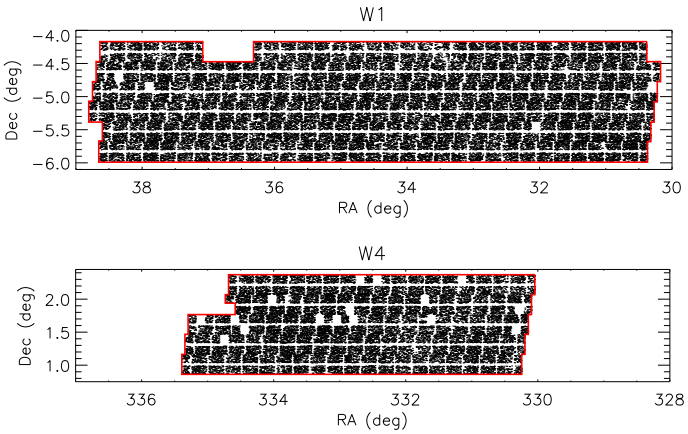

Fig. A.1. RA-Dec distribution of secure redshift galaxies in W1 (*top*) and W4 (*below*). The red thick line in each panel is the "field boundary" that we consider in this work. The cross-like pattern of void regions is due to the characteristic footprint of the VIMOS instrument. Rectangular empty regions are missing quadrants that have been discarded due to too poor observational conditions or technical problems.

5) Gaps and survey boundaries. As extensively discussed in Cucciati et al. (2014), we fill the cross-like pattern ("gaps") typical of VIMOS observations using the galaxies with photometric redshifts, to which we apply the ZADE method. The same holds for the empty regions corresponding to missing quadrants. In contrast, we take into account the "field boundaries" (the true limits in RA and Dec of the surveyed area, in red in Fig. A.1) as follows: when a cell falls partially outside the field boundaries, we divide $\rho(\boldsymbol{r})$ by the fraction of the filter that falls within the boundaries before computing $\delta(\boldsymbol{r})$ (see Cucciati et al. 2006).

6) Mean density. We compute the mean density $\langle\rho(\mathbf{r}(z))\rangle$ by smoothing the VIPERS $n(z)$ with a statistical approach based on the $V_{\rm max}$ method. Full details are given in Kovač et al. (2010) (but see also Marulli et al. 2013; and de la Torre et al. 2013). In the case of the spherical filter (which is based on a 3D distance), we then compute $\langle\rho(\boldsymbol{r}(z))\rangle$ dividing the $n(z)$ by the volume of the survey. In the case of cylindrical filters, we obtain $\langle\rho(\boldsymbol{r}(z))\rangle$ by integrating $n(z)$ in a redshift range of $\pm 1000\,{\rm km\,s^{-1}}$ centred on the redshift of each given galaxy and by dividing the result by the survey area.

A.2. ZADE

We use a modified version of the ZADE approach described in Kovač et al. (2010). All the details of the performance of ZADE in a VIPERS-like survey with respect to other methods are given in Cucciati et al. (2014). Cucciati et al. (2014) tested the performance of the method using spherical cells. Since the performance is not expected to depend on the filter shape, we adopted the same method here.

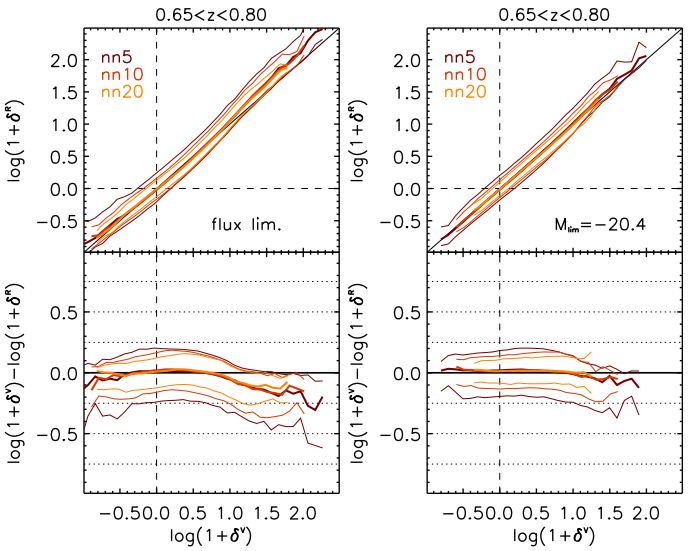

Fig. A.2. Comparison of δ^R and δ^V on a galaxy-by-galaxy basis. Results are shown for the cylindrical filter with radius corresponding to the fifth, tenth, and twentieth n.n. for the redshift bin $0.65 < z < 0.8$. The density is computed using flux-limited tracers (*left*) and volume-limited tracers with $M_{\rm lim} = -20.4$ (*right*). x-axis: density contrast in the VMOCKS; y-axis, *top panel*: density contrast in the RMOCKS; y-axis, *bottom panel*: difference of the logarithms. The thick lines are the median value of the quantity displayed on the y-axis in each x-axis bin. Thin lines represent the sixteenth and eightyfourth percentiles of its distribution. The solid black line in the top panels is the one-to-one line, and the horizontal lines in the bottom panels are for reference.

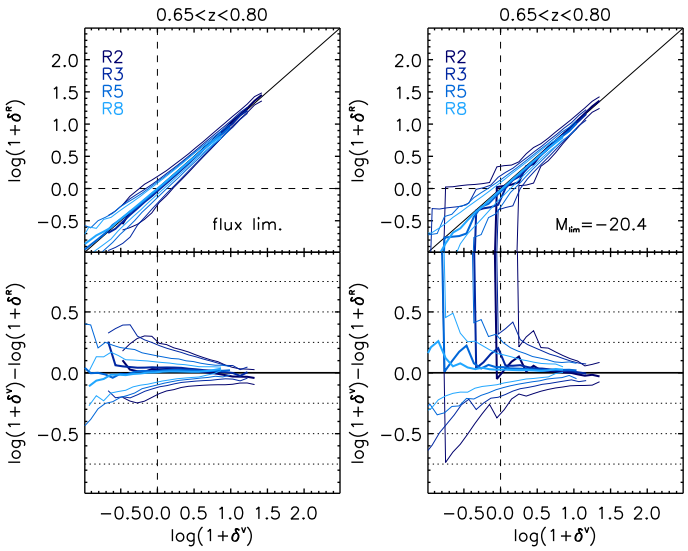

Fig. A.3. As in Fig. A.2, but for cylinders with fixed radius.

The method is applied to each galaxy for which we have only the photometric redshift, and it can be described as follows. For each of these galaxies, we keep its position in the sky (RA and Dec), and we collapse the probability distribution function (PDF) of its photometric redshift $z_{\rm P}$ on several probability peaks along the l.o.s. The redshifts of these peaks are determined by the peaks of the $n(z)$ of the spectroscopic galaxies falling in a cylinder centred on the position of the given photometric galaxy (RA, Dec and $z_{\rm p}$), with radius $R_{\rm ZADE} = 5\,h^{-1}$ Mpc and half-length equal to $3\sigma_{z\rm p}$. The weights $w_{\rm ZADE}$ assigned to these peaks are given by the product of the PDF by $n(z)$, normalised to unity.

By applying this method, the summation in Eq. (2) runs over all the spectroscopic galaxies setting $\phi = 1$ and over all the peaks setting ϕ equal to each given $w_{\rm ZADE}$. Counts are performed only among the galaxies that satisfy the selection criteria to be considered as tracers for both spectroscopic and photometric galaxies.

A.3. Reliability of the density reconstruction

We compute the density contrast δ in the RMOCKS and VMOCKS (δ^R and δ^V, respectively) using Eqs. (1) and (2). In the RMOCKS the filter is centred on all the galaxies, and the summation in Eq. (2) runs on all the tracers, each with $\phi = 1$. In the VMOCKS we centre the filters only around spectroscopic galaxies, and we apply the ZADE method. This way, the summation in Eq. (2) runs over all the spectroscopic galaxies with $\phi = 1$, and over all the ZADE peaks, for each setting $\phi = w_{\rm ZADE}$. Then we match each RMOCK with the spectroscopic catalogue of its corresponding VMOCK, to have δ^R and δ^V measured for the same set of galaxies[7].

We compare δ^R and δ^V in two ways: on a galaxy-by-galaxy basis, to assess how well we can recover the density absolute value, and according to their ranking, to assess how well we can separate low- and high-density regions. We performed the comparison in three redshift bins, the same used for the scientific analysis of this paper: $0.51 < z \leq 0.65$, $0.65 < z \leq 0.8$, and $0.8 < z \leq 0.9$. We note that the results of this comparison depend very mildly on redshift, therefore we only show the results for the central redshift bin here.

Figures A.2 and A.3 show the galaxy-by-galaxy comparison. We show only the cases of the flux-limited sample and the brightest volume-limited sample, as they represent the two most extreme types of tracers. We note that for fixed radius and volume-limited tracers (right panels in Fig. A.3) the sharp discontinuity to infinity is an artefact corresponding to the case of zero counts. We see that

- for both the adaptive and fixed radii, the systematic error is always close to zero except for the highest densities in the case of flux-limited and adaptive radius, where we underestimate the real density by ∼30%.
- The random error does not depend on density for the adaptive radii, and it varies between ∼40% and ∼15% from $R_{\rm 5th}$ to $R_{\rm 20th}$; in contrast, it depends on density for the fixed radii, dropping from >40% to ∼10% when moving from low to high density. This different behaviour is due to fixed or varying number of galaxies within the cylinders in the case of the adaptive or fixed radius, respectively.
- In all cases, the random error is smaller for larger radii, and neither the systematic nor the random error seems to depend on redshift.

We note that one of the reasons why the high densities are underestimated is that VIPERS is a single-pass survey, so that close pairs are more difficult to target (unless the two galaxies are so close and at the same Dec that they fall in the same slit). The use of ZADE partially mitigates this loss because it allows us to use all the not-targeted galaxies (although with a larger error on the position along the l.o.s.).

[7] To assess the reliability of the VIPERS density field reconstruction, we used also a set of light cones derived with a HOD method as described in de la Torre et al. (2013), which are the same used in Cucciati et al. (2014) and D16. The results obtained with these HOD mock catalogues are very similar to the result described here, therefore we do not show them.

Table A.1. Completeness and contamination for LD and HD quartiles for different types of filter and different radii and tracers.

Filter	Completeness (%)		Contamination (%)	
	LD	HD	LD	HD
Volume-limited tracers ($M_{\rm lim} = -20.4$)				
$R_{5\rm th}$	73.8	74.1	<1	<1
$R_{10\rm th}$	75.9	76.7	<1	<1
$R_{20\rm th}$	77.8	78.4	<1	<1
$R_{2\rm c}$	68.8	74.0	<1	<1
$R_{3\rm c}$	70.5	76.2	<1	<1
$R_{5\rm c}$	75.9	79.8	<1	<1
$R_{8\rm c}$	80.2	82.7	<1	<1
Flux-limited tracers				
$R_{5\rm th}$	74.1	74.9	1.1	<1
$R_{10\rm th}$	76.6	78.7	<1	<1
$R_{20\rm th}$	78.8	81.3	<1	<1
$R_{2\rm c}$	70–75	76–82	<1	<1
$R_{3\rm c}$	74–78	78–84	<1	<1
$R_{5\rm c}$	78–83	81–87	<1	<1
$R_{8\rm c}$	82–87	84–88	<1	<1

Notes. Values represent the average over the three redshift bins when the spread among the three values was below 3%, otherwise the minimum and maximum values are given.

We also performed a less demanding test: we compared the δ^R and δ^V values according to their ranking, and not to their value. We divided δ^R and δ^V into quartiles, and we focused on the first quartile (the lowest densities, "LD"), and the last quartile (the highest densities, "HD").

We call N_i^V (N_i^R) the number of galaxies falling in the percentile i of the δ^V (δ^R) distribution, with i equal to LD or HD. Also, we call $N_{i,j}^{V,R}$ the number of galaxies that fall in the percentile i of δ^V and in the percentile j of δ^R, with j also equal to LD or HD. We then define the completeness and contamination of the percentile i as

$$\text{completeness} = N_{i,i}^{V,R}/N_i^R \quad (A.1)$$

$$\text{contamination} = N_{i,j}^{V,R}/N_i^V \qquad (\text{with } i \neq j). \quad (A.2)$$

In practice, the completeness expresses the fraction of galaxies that are placed in the correct percentile, while the contamination indicates which fraction of galaxies belonging to the LD(/HD) percentile of δ^V distribution come from the opposite percentile HD(/LD) of the original δ^R distribution. The best result would be a completeness of 100% and a contamination equal to zero.

The values of completeness and contamination for the different types of filters and radii are shown in Table A.1. We find that the values of completeness and contamination mirror the results shown in Figs. A.2 and A.3, and they mainly depend on the random error shown in these figures. The relatively low random errors allows us to obtain quite high levels of completeness (almost always above 75%), and basically zero contamination. Moreover, for cylinders with a fixed radius, the completeness is higher in HD than in LD, corresponding to the larger random error in LD.

We conclude that we can distinguish with confidence between the lowest and highest density regions, each time selecting highly complete samples with very low contamination from the opposite environment. This is particularly important for the scientific analysis in this paper.

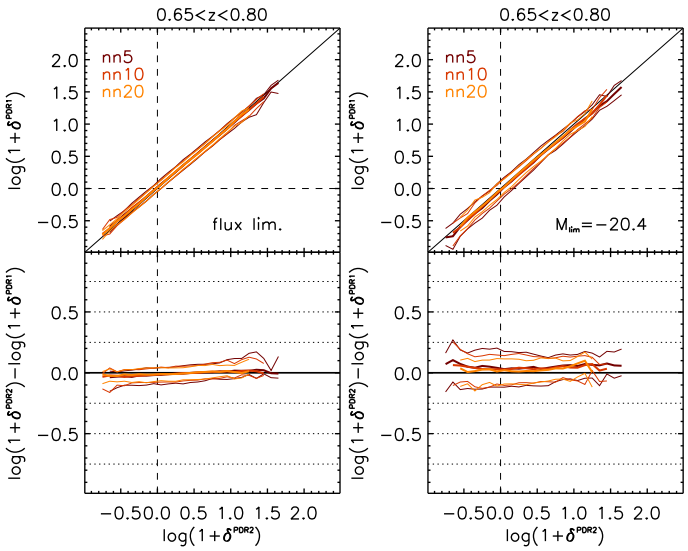

Fig. B.1. As in Fig. A.2, but here we compare the density field in the VIPERS PDR-1 sample and the density field used in this paper (for simplicity indicated as PDR-2 in the labels).

Appendix B: Density field in the PDR-1

In this appendix we compare the density field computed for the VIPERS PDR-1 sample, used in D16, with the density field that we use in this paper. The comparison is shown in Fig. B.1 for the galaxies in common to both the samples. We only show one redshift bin because the results in the two other bins are very similar. The systematic difference is almost zero, and the scatter around the mean difference is $\lesssim$10% for the flux-limited tracers and $\lesssim$25% for the volume-limited tracers. In both cases, it is smaller than the random error in the density field reconstruction due to the VIPERS observational strategy (Fig. A.2). We also remark that the systematic and random errors are both smaller for larger radii.

Appendix C: sSFR distribution in the model

In Fig. 3 we have shown that the sSFR distribution in the model is different from the data distribution in several aspects. We verified whether these differences could be due to the lack of measurement errors in the model sSFR by adding an error to the model stellar mass or to the model SFR or to both of them, extracted from a Gaussian distribution with $\sigma = 0.25$ (dex).

Firstly, we analysed the tail of high sSFR, which is missing in the model. By adding the error only to the stellar mass, the tail of high sSFR shrinks even further, as expected. In fact, if we add a Gaussian error to the stellar mass, given the shape of the GSMF, galaxy masses are preferentially boosted. We therefore expect the sSFR to decrease. Instead, if we also add an error to the SFR, the high-sSFR tail of the sSFR distribution tends to increase as we increase the SFR error. In this way, we can recover the observed tail of high sSFR. We remark that the model and observed sSFR tails are increasingly similar at higher redshift, so that we would need to use different SFR errors at different redshifts to match the models to the observations. Moreover, if we consider the two errors on stellar mass and on SFR to be correlated, the overall shape of the model sSFR is preserved (e.g., the sort of plateau at $\log(sSFR) \sim -11$), while when we use uncorrelated errors, the sSFR distribution becomes smoother, assuming the shape of a single-peaked skewed distribution.

Secondly, the data sSFR distribution features a valley at $\log(sSFR) \sim -10.8$, whereas the model predicts a plateau. We are unable to reproduce this valley by adding an error to the model stellar mass and SFR. Correlated errors do not alter the shape of this plateau, while uncorrelated errors removed the point of inflection altogether.

Although by adding these measurement errors we obtain a better agreement between the model and the observed sSFR distributions, we decided not to include them in the model sSFR because modelling them accurately is beyond the scope of this paper.

Given the different shape of the model and observed sSFR distributions, we do not use the thresholds $\log(sSFR) < -11.2$ and $\log(sSFR) > -10.8$ (used for the VIPERS data, see Sect. 4.1) to define passive and active galaxies in the model. Instead, in each redshift bin, considering only galaxies above the mass limit, we computed the fraction of passive and active galaxies in the data (defined using the sSFR thresholds). We used the same fractions in the model, starting to count galaxies from the two tails of the sSFR distribution. The comparison between the data and the model should be more meaningful when we select the same "extremes" of the sSFR distribution. In the data, the fraction of passive galaxies ranges from 35% to 44% from the lowest to the highest redshift bin, and the fraction of active galaxies ranges from 52% to 40%. In the model, these fractions of passive galaxies roughly correspond to selecting all galaxies with $\log(sSFR) < -11.66, -11.30, -11.23$ from the lowest to the highest redshift. The fractions of active galaxies correspond to a selection given by $\log(sSFR) > -10.7, -10.5$, and -10.4.

We note that we compute these fractions considering only the galaxies above the stellar mass limit in each redshift bin. This is because, as shown in Davidzon et al. (2013), the model GSMFs are more similar to those in VIPERS for $\log(\mathcal{M}/\mathcal{M}_\odot) \gtrsim 10.7$. This allows us to work within a stellar mass range where our model and the data are in better agreement.